The Astrophysical Journal Supplement Series, 255:18 (20pp), 2021 July https://doi.org/10.3847/1538-4365/ac00b6

Hidden Treasures in the Unknown 3CR Extragalactic Radio Sky: A Multiwavelength Approach

V. Missaglia[1,2,3,12], F. Massaro[1,2,3], E. Liuzzo[4], A. Paggi[1,3], R. P. Kraft[5], W. R. Forman[5], A. Jimenez-Gallardo[1,2,3,6], J. P. Madrid[7], F. Ricci[8,9], C. Stuardi[8,9], B. J. Wilkes[5], S. A. Baum[10], C. P. O'Dea[10], J. Kuraszkiewicz[5], G. R. Tremblay[5], A. Maselli[11], A. Capetti[2], E. Sani[6], B. Balmaverde[2], and D. E. Harris[5,13]

[1] Dipartimento di Fisica, Università degli Studi di Torino, via Pietro Giuria 1, I-10125 Torino, Italy
[2] INAF–Osservatorio Astrofisico di Torino, via Osservatorio 20, I-10025 Pino Torinese, Italy
[3] INFN–Istituto Nazionale di Fisica Nucleare, Sezione di Torino, I-10125 Torino, Italy
[4] INAF–IRA, via Piero Gobetti 101, I-40129, Bologna, Italy
[5] Center for Astrophysics | Harvard & Smithsonian, 60 Garden Street, Cambridge, MA 02138, USA
[6] European Southern Observatory, Alonso de Córdova 3107, Vitacura, Casilla 19001, Santiago de Chile, Chile
[7] University of Texas–Rio Grande Valley, One West University Boulevard, Brownsville, TX 78520, USA
[8] Dipartimento di Fisica e Astronomia, Università di Bologna, via Piero Gobetti 93/2, I-40129 Bologna, Italy
[9] INAF–Osservatorio di Astrofisica e Scienza dello Spazio di Bologna, Via Piero Gobetti, 93/3, I40129 Bologna, Italy
[10] University of Manitoba, Dept. of Physics and Astronomy, Winnipeg, MB R3T 2N2, Canada
[11] Space Science Data Center–Agenzia Spaziale Italiana, Via del Politecnico, snc, I-00133, Roma, Italy
Received 2021 February 23; revised 2021 April 26; accepted 2021 May 11; published 2021 July 19

Abstract

We present the analysis of multiwavelength observations of seven extragalactic radio sources, listed as unidentified in the Third Cambridge Revised Catalog (3CR). X-ray observations, performed during Chandra Cycle 21, were compared to Very Large Array (VLA), Wide-field Infrared Survey Explorer, and Pan-STARRS observations in the radio, infrared, and optical bands, respectively. All sources in this sample lack a clear optical counterpart, and are thus missing their redshift and optical classification. In order to confirm the X-ray and infrared radio counterparts of core and extended components, here we present for the first time radio maps obtained manually reducing VLA archival data. As in previous papers on the Chandra X-ray snapshot campaign, we report X-ray detections of radio cores and two sources, out of the seven presented here, are found to be members of galaxy clusters. For these two cluster sources (namely, 3CR 409 and 3CR 454.2), we derived surface brightness profiles in four directions. For all seven sources, we measured X-ray intensities of the radio sources and we also performed standard X-ray spectral analysis for the four sources (namely, 3CR 91, 3CR 390, 3CR 409, and 3CR 428) with the brightest nuclei (more than 400 photons in the 2″ nuclear region). We also detected extended X-ray emission around 3CR 390 and extended X-ray emission associated with the northern jet of 3CR 158. This paper represents the first attempt to give a multiwavelength view of the unidentified radio sources listed in the 3CR catalog.

Unified Astronomy Thesaurus concepts: X-ray astronomy (1810); Active galaxies (17); Radio continuum emission (1340)

1. Introduction

The Third Cambridge Catalog of radio sources (3C; Edge et al. 1959) performed at 159 MHz, and its revised releases at 178 MHz (3CR, Bennett 1962; 3CRR, Laing et al. 1983; and the Spinrad et al. 1985 update) are paramount low-frequency radio catalogs for studying radio-loud, active galactic nuclei (AGNs) and their environments at all scales (see, e.g., Fabian 2012; Kraft et al. 2012; Liu et al. 2020). To a great degree, the success of this catalog is due to the fact that its latest revision (3CRR) has a flux limit of 9 Jy at 178 MHz and it represents a statistically complete sample of the most powerful radio galaxies, including a variety of extended radio morphologies, optical classes, and environmental properties.

On the basis of the 3CR radio observations at 178 MHz, Fanaroff & Riley (1974) proposed a classification for radio sources based on the relative position of regions of high and low surface brightness in their extended structures, distinguishing between FRI, i.e., edge-darkened, and FRII, i.e., edge-brightened, types. Since 1974, a lot more has been learned on the FRI/FRII dichotomy, as reported in Bridle (1984), Baum et al. (1995), Chiaberge et al. (2000), and Mingo et al. (2019). Between the 1980s and 1990s, an additional classification was proposed, on the basis of the relative intensity of high- and low-excitation lines in the optical spectra (Hine & Longair 1979; Laing et al. 1994). Two populations of radio galaxies were then defined: high-excitation radio galaxies (HERGs), and low-excitation radio galaxies (LERGs). These two classes are believed to represent intrinsically different types of objects, since they show different accretion rates (Chiaberge et al. 2002; Hardcastle et al. 2009; Best & Heckman 2012), host galaxies, and redshift evolution (Pracy et al. 2016).

In the past three decades, several photometric and spectroscopic surveys of 3CR radio sources have been carried out. For example, using the Hubble Space Telescope (HST), the 3CR catalog has been observed in the near-ultraviolet (Allen et al. 2002), optical (de Koff et al. 1996; McCarthy et al. 1997; Martel et al. 1999; Privon et al. 2008; Tremblay et al. 2009; Ramírez et al. 2017), and near-infrared (Madrid et al. 2006; Baldi et al. 2010). Buttiglione et al. (2009) carried out an optical spectroscopic survey of 3CR radio galaxies with the Telescopio Nazionale Galileo. More recently, Balmaverde et al. (2019) presented Very Large Telescope/Multi Unit Spectroscopic Explorer (VLT/MUSE) observations of 20 low-z 3CR

[12] Corresponding author.
[13] Passed on 2015 December 6.

radio galaxies. Finally, Very Long Baseline Array (VLBA) data for several 3CR objects at redshifts $z < 0.2$ were also obtained (see, e.g., Giovannini et al. 2001; Liuzzo et al. 2009, and references therein).

In X-rays, most of the 3CR extragalactic radio sources were observed with Chandra, XMM-Newton, and Swift (see, e.g., Worrall et al. 2001; Hardcastle et al. 2005; Kraft et al. 2007). Until Cycle 9 the Chandra archive covered only ∼60% of the 3CR extragalactic sample, while the other X-ray telescopes, such as XMM-Newton, had obtained data for less than one-third of the entire catalog.

In 2008, the 3C Chandra snapshot campaign began, aiming to detect X-ray emission in extragalactic radio sources arising from jets and hotspots, to determine their X-ray emission processes on a firm statistical basis, and to study the nuclear emission of the host galaxies (Massaro et al. 2010). In the Chandra archive, 150 out of 298 3CR extragalactic sources were already present before the beginning of the survey. We observed 123 3CR sources, and X-ray emission has been detected in 119 out of 122 radio cores, in addition to the discovery of the X-ray counterpart for eight jet knots, 23 hotspots, with marginal detection for another 9, and 17 radio lobes (see Jimenez-Gallardo et al. 2020 for the latest run of Chandra observations). Diffuse X-ray emission was also detected around several 3C radio sources, potentially associated with either their radio lobes or radiation arising from the intergalactic medium (IGM) when harbored in galaxy clusters/groups (see, e.g., 3C 17, 3C 196.1, 3C 89, and 3C 187; Dasadia et al. 2016; Madrid et al. 2018; Ricci et al. 2018; Paggi et al. 2021, respectively). Some of the most interesting 3CR sources have been investigated in more detail with Chandra follow-up observations, such as 3C 171, 3C 105, and 3C 305 to name a few (see, e.g., Hardcastle et al. 2010, 2012; Orienti et al. 2012, respectively). Additional Chandra X-ray observations, restricted to the 3CRR catalog, also have been carried out in parallel during the past decade (see, e.g., Wilkes et al. 2013).

During our campaign, we determined that 25 3CR sources out of 298 were optically unidentified, that is, lacking an optical counterpart of their core, and therefore have neither optical classification nor redshift (see Massaro et al. 2013). This means that there is no detected emission from the host galaxy in the optical band, and this could be due to multiple reasons. These sources might, in fact, be either high-redshift quasars/radio galaxies, or highly absorbed/obscured lower-z active galaxies, or optically faint LERGs, that lack radiatively efficient AGN signatures in the optical emission. (See Section 3 for more information on individual sources properties.)

This warranted follow-up observations.

Maselli et al. (2016) carried out an optical-to-X-ray campaign that includes data from the Swift Observatory. These authors found that a total of 21 out of the 25 unidentified sources observed by Swift have an National Radio Astronomy Observatory (NRAO) Very Large Array (VLA) Sky Survey (NVSS; Condon et al. 1998) counterpart. Thirteen of them also show mid-infrared (IR) emission as detected in the AllWISE (Wide-field Infrared Survey Explorer mission; Wright et al. 2010) Source Catalog, and 9 out of these 21 sources have an X-ray counterpart detected in the 0.5–10 keV energy range, above 5σ level of confidence.

In this paper, we present the results of Chandra follow-up observations for seven of the nine unidentified 3C sources with the Swift X-ray counterpart, all observed in 2020. The two remaining sources are expected to be observed in 2021 April, according to the Chandra long-term schedule,[14] and their analysis will be presented in a forthcoming paper (V. Missaglia et al. 2021, in preparation).

Here, we also present, for the first time, radio observations available for the selected sample in the historical VLA archive. Both radio and X-ray observations are also compared with data collected with the Panoramic Survey Telescope & Rapid Response System (Pan-STARRS; Chambers & Pan-STARRS Team 2016) and Wide-field Infrared Survey Explorer (WISE; Wright et al. 2010).

The paper is organized as follows. A brief overview of the data reduction procedures, both for the radio and X-ray band, is given in Section 2, while results on single sources are discussed in Section 3. In Section 4 we present our summary and conclusions. In the Appendix, we show all the radio maps we obtained from the historical VLA archive.[15]

Unless otherwise stated, we adopt cgs units for numerical results and we also assume a flat cosmology with $H_0 = 69.6$ km s^{-1} Mpc^{-1}, $\Omega_M = 0.286$, and $\Omega_\Lambda = 0.714$ (Bennett et al. 2014). Spectral indices, α_X, are defined by flux density, $S_\nu \propto \nu^{-\alpha_X}$. WISE magnitudes in the nominal bands at 3.4 (W1), 4.6 (W2), 12 (W3), and 22 (W4) μm are in the Vega system, while Pan-STARRS1 adopts the AB magnitude system (Oke & Gunn 1983).

2. Data Reduction and Analysis

To search for optical and infrared counterparts of our selected targets, we first retrieved all radio observations from the historical VLA archive, aiming at detecting their radio cores. After data reduction, we overlaid radio contours on optical, IR, and X-ray images. In Table 1 we report (1) 3C designation, (2)–(3) coordinates in J2000 Equinox, (4) Galactic absorption as reported in Kalberla et al. (2005), (6) Chandra observation ID and date, (7) flux at 178 MHz retrieved from Spinrad et al. (1985), and (8)–(11) remarks on the sources from this work.

2.1. Radio Archival Observations

All radio data presented in this paper were retrieved from the historical VLA Archive managed by the NRAO. A summary of all radio observations is presented in Table 2 where we report (1) 3C designation, (2) NRAO observing project identification, (3) observing band, (4) spectral windows, (5) telescope configuration in which the observation was performed, (6) clean beam size, (7) total flux of the source, (8) peak flux of the radio image, (9) observation time on source, (10) rms noise of the clean image, and (11) contour levels used in the radio maps.

Calibration and imaging were performed in CASA[16] v5.1.1-5 (McMullin et al. 2007) adopting manual standard procedures. For each source, whenever possible, we reduced observations in the L, C, and X radio bands (at 1.5, 6, and 10 GHz nominal frequencies, respectively). For all bands, after inspecting the observation log, we manually flagged antennas with bad data. Then, we performed the calibration adopting the following steps: (1) we provided a flux density value for the amplitude calibrator, (2) we derived corrections for the complex antenna gains, (3) we used the flux calibrator to determine the system

[14] https://cxc.harvard.edu/target_lists/longsched.html
[15] https://science.nrao.edu/facilities/vla/archive/index
[16] https://casa.nrao.edu/

response to a source of known flux density, and finally (4) we applied the calibrations to our calibrators and our target. Bandpass correction is not necessary given that all observations are performed in single channel mode. As a last step, we performed self-calibration, changing the weight parameter in every step of the cleaning process to recover all the extended emission, and setting manual boxes.

2.2. X-Ray Observations

Chandra data reduction and analysis have been carried with the Chandra Interactive Analysis of Observations (CIAO, v4.11; Fruscione et al. 2006) following the standard procedures and threads.[17] We also used the Chandra Calibration Database v4.8.2, according to the same method adopted in our previous investigations of the 3CR snapshot observations (see, e.g., Massaro et al. 2010, 2011 for additional information). Only a brief overview of the reduction process is reported below.

We performed the astrometric registration between radio and X-ray images by aligning the X-ray position of each core with that of the radio images, as in previous papers on the 3CR Chandra Snapshot Survey (see Massaro et al. 2011, 2012, 2018; Stuardi et al. 2018). In Table 3, we report the radio/X-ray shift, which for all sources is less than 2″, corresponding to ∼90% of the Chandra point-spread function (PSF). 3CR 409 is the only source out of the seven presented in this work that could not be registered due to the lack of a radio core detection. WISE and Pan-STARRS data sets are not registered to the radio position, as done for the X-ray data; thus small shifts (i.e., less than ∼1″) may be seen when overlaying radio contours on IR and optical images, consistent with their astrometric uncertainty[18] and seeing in the Pan-STARRS case (Magnier et al. 2020). However this does not affect associations of radio and X-ray nuclei with their mid-IR and optical counterparts since below ∼1″ the chance probability of a spurious association is less than 0.1% (see, e.g., Massaro et al. 2014; D'Abrusco et al. 2019 for details).

2.2.1. X-Ray Photometry

We used unbinned and unsmoothed X-ray images restricted to the 0.5–7 keV band to search for the X-ray nuclei. X-ray detection significance, reported as Gaussian equivalent standard deviation (σ), was estimated measuring the number of photons in both the nuclear region, if present, and a background region. The background region was chosen to be a circular aperture with a radius of 10″, i.e., 5 times larger in radius than the one used for the X-ray detection of nuclei, and located far enough from the radio galaxy (i.e., at least a few tens of arcseconds) to avoid the off-axis degradation of the PSF on charge coupled device borders and contamination from the source, if extended. Adopting a Poisson distribution for the number of photons in the background, we computed the level of significance for X-ray excesses associated with the position of radio cores, if any. For 3CR 409, where no registration was possible, we centered the nuclear regions at the position corresponding to the emission peak in the 4–7 keV band.

We also created flux maps in the X-ray energy ranges 0.5–1 keV (soft), 1–2 keV (medium), and 2–7 keV (hard), taking into account both exposure maps and effective areas. To this end, we used monochromatic exposure maps set to the nominal energies of 0.75, 1.4, and 4 keV for the soft, medium, and hard bands, respectively. All flux maps were converted from units of counts $cm^{-2}\,s^{-1}$ to cgs units by multiplying each map pixel by the nominal energy of each band. We made the necessary correction to recover the observed $erg\,cm^{-2}\,s^{-1}$, when performing X-ray photometry (see, e.g., Hardcastle et al. 2012; Madrid et al. 2018 for details). This is the same procedure adopted for X-ray photometry in all previous analyses of our 3CR Chandra Snapshot Survey (see, e.g., Massaro et al. 2015; Stuardi et al. 2018; Jimenez-Gallardo et al. 2020).

Flux maps were then used to measure observed fluxes for all the X-ray detected nuclei and extended components associated with radio structures. Uncertainties are computed assuming Poisson statistics (i.e., square root of the number of counts) in the source and background regions. X-ray fluxes for the cores are not corrected for the Galactic absorption, and are reported in Table 4.

2.2.2. X-Ray Surface Brightness Profiles

For 3CR 409 and 3CR 454.2, we detected significant diffuse X-ray emission in the 0.5–7 keV band, extending beyond the radio structure. Thus, to estimate the extension of this X-ray emission, we derived its surface brightness profiles, reported in Section 3).

First, we detected and removed X-ray pointlike sources (including the X-ray nuclei of the radio galaxies) in the 0.5–7 keV images using the WAVDETECT task, available in CIAO. We adopted a sequence of $\sqrt{2}$ wavelet scales, from 1 to 16 to cover different sized sources, and a false-positive probability threshold set to the value of 10^{-6}, which is the value recommended for a 1024×1024 image in the CIAO threads.[19] This value was chosen to ensure that we do not oversubtract point sources. We generated the corresponding source regions using the ROI task.[20]

We computed the 0.5–7 keV, exposure-corrected X-ray surface brightness profiles in four quadrants (north, south, east, and west). The background was estimated as a circular region of ∼80″ radius, far from the source, and free of detected sources. A similar procedure was used in Jimenez-Gallardo et al. (2021) to search for X-ray counterparts of radio hotspots.

2.2.3. X-Ray Spectral Analysis

We performed spectral analysis for the X-ray counterparts of radio cores of four sources having more than 400 photons (as reported in Table 4) within a circular region of 2″, centered on the radio core position (namely, 3CR 91, 3CR 390, 3CR 409, and 3CR 428) and in more extended regions corresponding to X-ray diffuse emission. This analysis was carried out to determine X-ray spectral indices α_X, the presence of significant intrinsic absorption, if any, and to estimate the temperature, abundances, and density for the intracluster medium (ICM) of the two galaxy clusters detected (namely, 3CR 409 and 3CR 454.2).

The spectral data for the X-ray cores were extracted from a 2″ aperture, as for photometric measurements, using the CIAO routine SPECEXTRACT, thereby automating the creation of

[17] http://cxc.harvard.edu/ciao/threads/

[18] https://wise2.ipac.caltech.edu/docs/release/allwise/ and https://panstarrs.stsci.edu.

[19] https://cxc.harvard.edu/ciao/threads/wavdetect/

[20] https://cxc.cfa.harvard.edu/ciao/ahelp/roi.html

count-weighted response matrices. In the cases of the sources hosted in clusters, namely, 3CR 409 and 3CR 454.2, we have extracted the spectrum from a circular region of $\sim 1'$ excluding a $2''$ aperture covering the nucleus. Background spectra were extracted in nearby circular regions of radius $80''$ free of detected sources. The source spectra were then filtered in energy between 0.5 and 7 keV and binned to allow a minimum number of 20 counts per bin to ensure the use of the χ^2 statistic. We used the SHERPA[21] (Freeman et al. 2001) modeling and fitting package to fit our spectra.

For the nuclear spectra, as performed in all our previous analyses of sources observed during the 3CR Chandra Snapshot Survey, we adopted an absorbed power-law model with the hydrogen column density $N_{\rm H}$ fixed at the Galactic values and a contribution of intrinsic absorption (xswabs*xszwabs*xspowerlaw). In the following section, we report the values obtained by our best fits. When considering the fitting model, the two main free parameters—namely, the intrinsic absorption $N_{\rm H,int}$ and the spectral index $\alpha_{\rm X}$—were allowed to vary, to quantify the degree to which $N_{\rm H,int}$ and $\alpha_{\rm X}$ are degenerate. In all cases, we adopted the photometric redshift obtained from WISE counterpart magnitudes, as described in Glowacki et al. (2017). These authors, using the WISE two-color plot (W1–W2 versus W2–W3), were able to distinguish LERGs (typically associated with passive elliptical galaxies), HERGs (associated with smaller but higher star-forming galaxies hosting radiative AGNs), and QSOs. The method described to estimate the redshift offers, therefore, also the probability of a radio source to be either a LERG, or a HERG, or a QSO, using the kernel density estimation (KDE; for more information about this method see Section 2.2 in Glowacki et al. 2017). These probabilities are used to weight the redshift estimation made for each class (see Table 2 in Glowacki et al. 2017). In Table 5 photometric redshifts and results of the X-ray spectral analysis of the cores are reported.

For 3CR 91, from the pileup map generated through the CIAO task pileup_map, we estimated the amount of pileup to be ∼15%. For this reason, before performing the spectral analysis of the X-ray counterpart of the radio core, we excluded the pixels most affected by the pileup (five pixels), obtaining a better fit with respect to the one adopting the jdpileup[22] model.

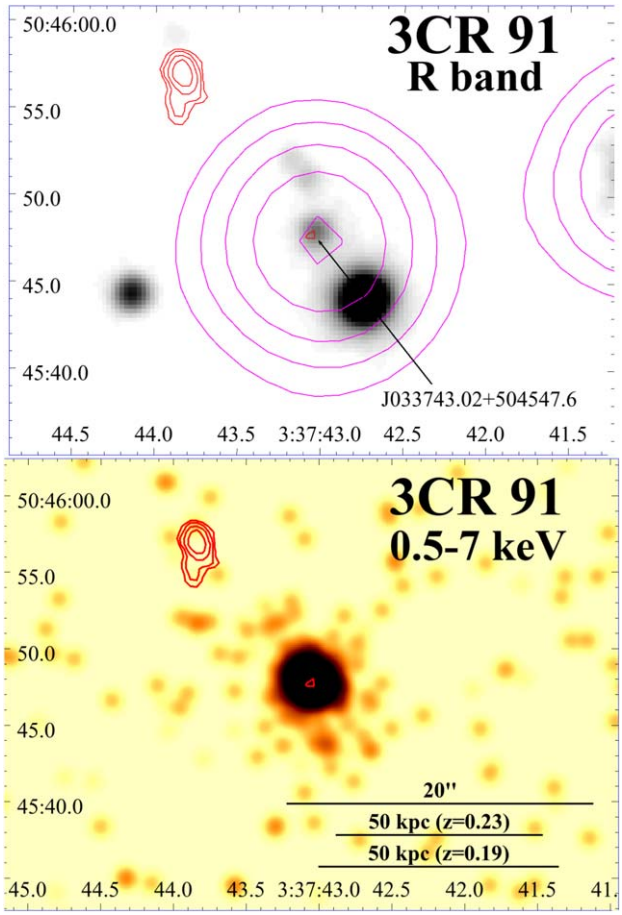

Figure 1. Upper panel: Pan-STARRS *R*-band image with WISE 3.4 μm filter magenta contours of the IR counterpart of the radio source overlaid. IR contours are drawn at 12.54, 16.91, 22.89, 31.07, and 42.27 in arbitrary flux scale. In red, 8 GHz VLA contours are shown, the same used in the Chandra image. The four radio contour levels were computed starting at 0.01 Jy beam^{-1}, increasing by a factor of 2. The arrow points to the WISE counterpart of the radio core. Lower panel: 0.5–7 keV Chandra image of 3CR 91 with VLA 8 GHz contours overlaid. The image has not been rebinned, but smoothed with a 3 pixel (equivalent to $1\farcs48$) Gaussian kernel. In the bottom right of the image, kiloparsec scales measured using the photometric redshifts obtained using the method described in Glowacki et al. (2017) are indicated.

3. Results and Details on Individual Sources

3.1. 3CR 91

From the historical VLA archive, we retrieved radio observations of 3CR 91 performed at 1.4 and 8 GHz in B and AB configurations, respectively. In the 8 GHz image (see red contours in the panels of Figure 1 and right panel of Figure A1) the radio core is clearly detected (i.e., above 5σ confidence level), while in the VLA image at 1.4 GHz (see Figure A1, left panel) the radio core is not visible. 3CR 91 is a double-lobed radio source in the VLA image at 1.4 GHz. On the other hand, in the 8 GHz radio map, we did not detect the emission arising from the southern radio lobe, clearly seen at lower frequencies, but the northern lobe resembles an FRII radio galaxy.

We found both the IR and the optical counterpart of the radio core in the Pan-STARRS and WISE images, as shown in the upper panel of Figure 1. The WISE counterpart to the core, J033743.02+504547.6, detected in all IR filters, is clearly the same object found within the Swift-XRT uncertainty circle, at small angular separation ($1\farcs4$) from its radio position. This source, as reported in Maselli et al. (2016), has an associated NVSS counterpart, J033743+504552. The WISE counterpart is included in D'Abrusco et al. (2014) all-sky catalog of infrared selected, radio-loud active galaxies, due to its peculiar infrared colors, and also in D'Abrusco et al. (2019). Since 3CR 91 has a WISE counterpart, adopting the method described in Glowacki et al. (2017), we were able to obtain a photometric redshift estimate of $z = 0.23 \pm 0.18$ from the 3.4 μm magnitude, and an estimate of $z = 0.19^{+0.18}_{-0.14}$ from the 4.6 μm magnitude, with 82% probability of being a QSO. In the Chandra image (Figure 1, lower panel), there is a clear detection of the radio core in the 0.5–7 keV energy range. 3CR 91 also shows extended X-ray emission up to $\sim 9''$ from the nucleus. We did not detect any X-ray counterpart for hotspots and lobes.

Since for 3CR 91 the number of photons within a circular region of $2''$ radius, centered on the radio position, is larger than 400, we carried out a nuclear X-ray spectral analysis. We adopted an absorbed power-law model with the hydrogen column density $N_{\rm H}$ fixed at the Galactic value (see Table 1, column (4)). As

[21] http://cxc.harvard.edu/sherpa
[22] https://cxc.cfa.harvard.edu/sherpa/ahelp/jdpileup.html

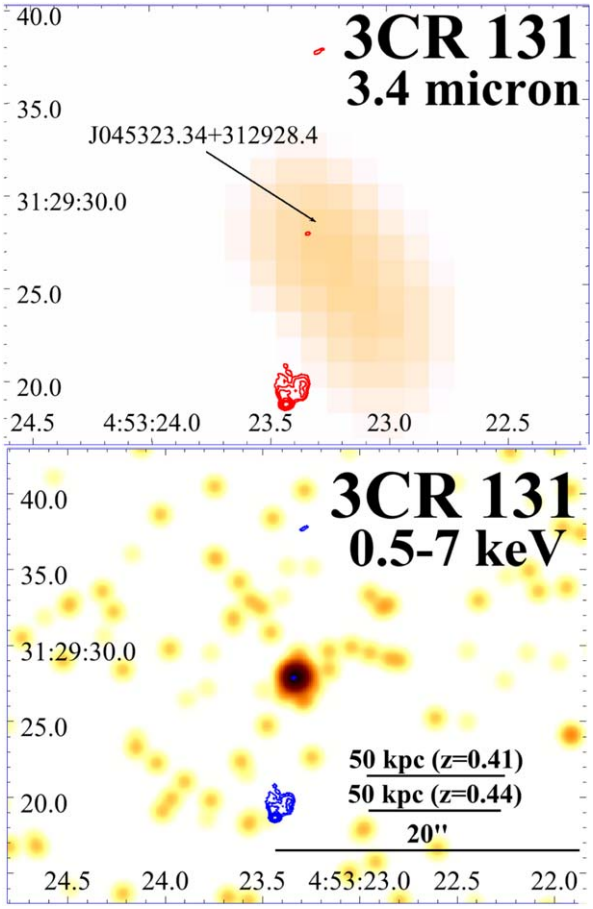

Figure 2. Upper panel: WISE 3.4 μm filter image of 3CR 131. The arrow points to the IR counterpart of the radio nucleus. No optical counterpart has been detected for this source. The six VLA 8 GHz radio contours levels (red) start from 0.002 Jy beam^{-1} and are increased by a factor of 2. Lower panel: 0.5–7 keV Chandra image of 3CR 131, with VLA 8 GHz band contours overlaid in red. Chandra image is not rebinned, but has been smoothed with a 5 pixel (2.″46) Gaussian kernel. In the bottom right of the image, kiloparsec scales measured using the photometric redshifts obtained using the method described in Glowacki et al. (2017) are indicated.

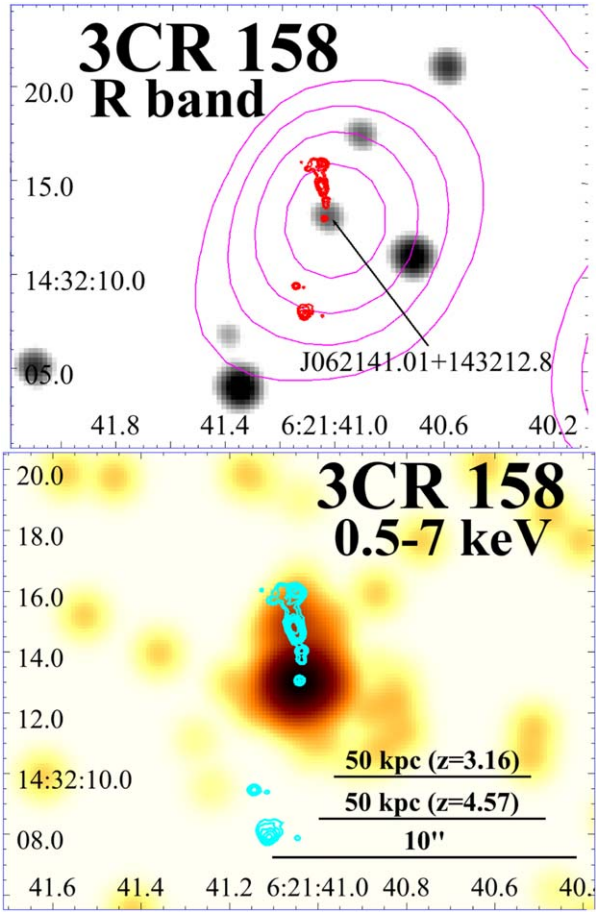

Figure 3. Upper panel: Pan-STARRS *R*-band image with WISE 3.4 μm filter magenta contours of the IR counterpart of the radio source overlaid. In red 8 GHz VLA contours are shown, the same used in the Chandra image (in cyan). VLA contours start from 0.002 Jy beam^{-1}, increasing by a factor of 2 up to 0.064 Jy beam^{-1}. IR contours are drawn at 13.40, 13.75, 14.21, 14.80 in arbitrary flux scale. The arrow points to the WISE counterpart of the radio core. Lower panel: Chandra X-ray image of 3CR 158 in the 0.5–7 keV energy band, binned to 0.″123/pixel and smoothed with a 5 pixel Gaussian kernel (equivalent to 0.″615). The northern radio jet has a clear X-ray counterpart. In the bottom right of the image, kiloparsec scales measured using the photometric redshifts obtained using the method described in Glowacki et al. (2017) are indicated.

reported in Table 5, for both photometric redshifts, we obtained the best-fit values setting $N_{\rm H,int}$ as free parameter, obtaining a value $\sim 10^{23}$ cm^{-2}, similar to that of the Galactic $N_{\rm H}$. Since 3CR 91 is a moderate-z QSO, we did expect a detection of the optical counterpart, in agreement with our results.

3.2. 3CR 131

For 3CR 131, we reduced VLA data at 8 GHz (see red radio contours in Figure 2, upper and lower panels) and at 1.4 GHz (see Figure A2, right panel). In the 8 GHz image, we detected the emission of both lobes and the nucleus, at 5 times the rms noise level, and a single radio hotspot in the southern lobe. The presence of the northern hotspot could suggest that 3CR 131 is an FRII radio galaxy. Using the method described in Glowacki et al. (2017), we obtained a photometric redshift estimate of $z = 0.41^{+0.13}_{-0.12}$ from the 3.4 μm magnitude value, and an estimate of $z = 0.4 \pm 0.13$ the 4.6 μm magnitude, and a 59% probability for this source to be an LERG.

We found the nuclear counterpart of 3CR 131 only in the IR image. In WISE W_1 filter (3.4 μm) image (see Figure 2, upper panel), there are two nearby objects at angular separation 4″∼ from the position of NVSS J045323+312924 (Maselli et al. 2016). Only one object, WISE J045323.34+312928.4 (indicated by an arrow in Figure 2, upper panel), is within the positional uncertainty of the Swift-XRT source. This WISE source is cospatial with the position of the nucleus in the 8 GHz radio map, and it is therefore likely its IR counterpart.

In the Chandra image (Figure 2, lower panel) the core is clearly detected and associated with the radio core, but the southern hotspot is not detected in the 0.5–7 keV energy range.

3.3. 3CR 158

3CR 158, at 8 GHz, is a lobe-dominated radio source (see red/cyan contours in Figure 3). The core is clearly detected in this band, as well as both the southern and northern lobes (see red and cyan contours in the upper and lower panels of Figure 3 and upper left panel of Figure A3). In particular, in the northern side there are two knots and one hotspot, hint that the source could be classified as FRII. The two knots in the southern radio structure are probably part of the same lobe but are not detected in the 4.5 GHz image (see Figure A3, upper right and bottom panels).

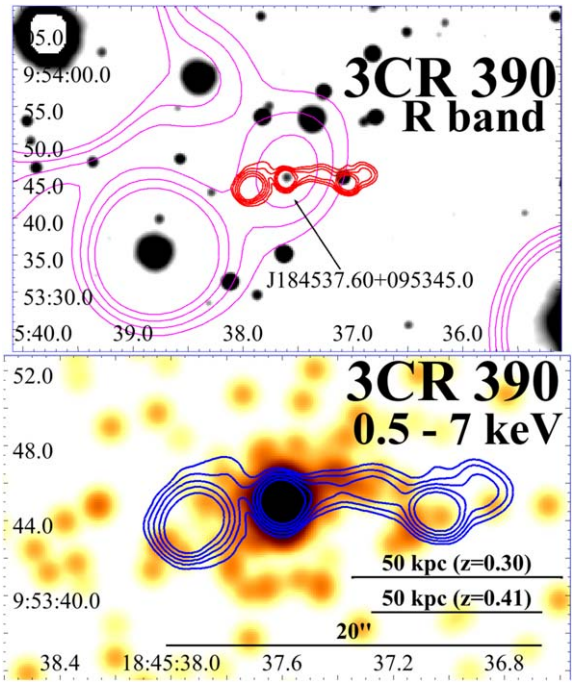

Figure 4. Upper panel: Pan-STARRS *R*-band image of the field of 3CR 390, with WISE 3.4 μm filter magenta contours overlaid. IR contours are drawn at 16.64, 19.28, 22.42, and 26.15 in arbitrary flux scale. VLA red contours at 4.5 GHz are overlaid, starting from 0.002 Jy beam^{-1} and increased by a factor of 2 up to 0.032 Jy beam^{-1}. The black arrow points to the position of the IR counterpart of the radio nucleus. Lower panel: Chandra X-ray image of 3CR 390 in the 0.5–7 keV band, binned to 0.″246/pixel and smoothed with a 5 pixel Gaussian kernel (equivalent to 1.″23). The X-ray image shows extended emission spatially coincident with the radio bridge in the western direction. In the bottom right of the image, kiloparsec scales measured using the photometric redshifts obtained using the method described in Glowacki et al. (2017) are indicated.

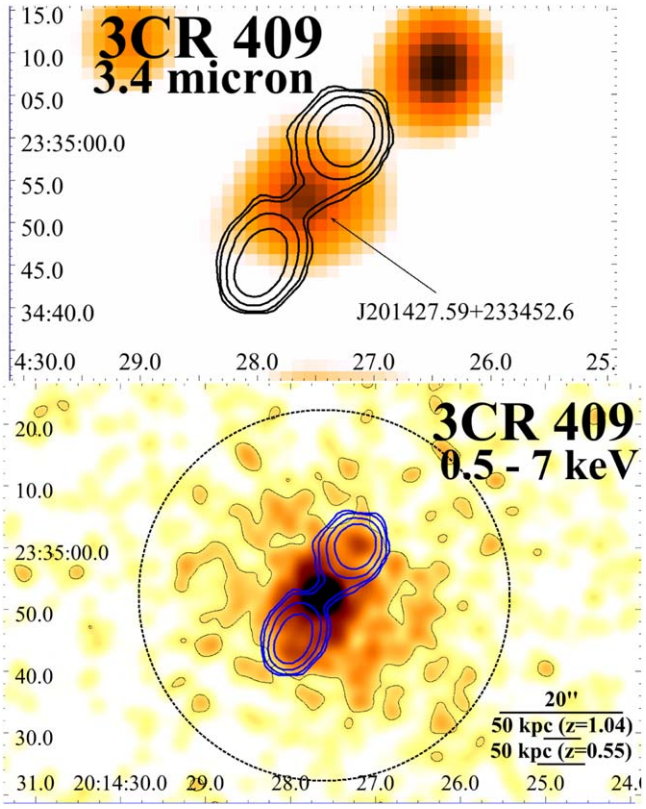

Figure 5. Upper panel: WISE 3.4 μm filter image of 3CR 409. The arrow points to the IR counterpart of the radio nucleus. No optical counterpart has been detected for this source. VLA red contours at 4.5 GHz are overlaid, starting from 0.02 Jy beam^{-1} increasing by a factor of 2, up to 0.64 Jy beam^{-1}. Lower panel: Chandra X-ray image of 3CR 409, filtered in the 0.5–7 keV band, rebinned to 0.″123/pixel and smoothed with a 4.″92 Gaussian kernel. VLA contours are the same as used in the upper panel. The dotted black circle has a 0.′5 radius. The black contours trace the X-ray emission at 3×10^{-18} erg cm^{-2} s^{-1}. The X-ray image shows emission associated with the radio lobes as well as more extended emission extending to 60″. In the bottom right of the image, kiloparsec scales measured using the photometric redshifts obtained using the method described in Glowacki et al. (2017) are indicated.

The core is also detected in both optical and IR images (see Figure 3, bottom panel). Maselli et al. (2016) reported that the X-ray source XRT J062141.2+143212 matches the NVSS source J062141+143211, within the 3C positional uncertainty region of 3CR 158. An infrared counterpart in the AllWISE Source Catalogue, WISE J062141.01+143212.8, is found at 1.″5 from the NVSS source, probably its counterpart (we remind that at these separations the chance probability of spurious association is below 0.1%). No infrared/optical candidate counterpart has been previously reported in the literature for this radio source. Adopting the procedure described in Glowacki et al. (2017), using the 3.4 μm WISE magnitude we obtained a photometric median redshift of $z = 4.57^{+0.68}_{-3.14}$ and using the 4.6 μm WISE magnitude, a photometric median redshift of $z = 3.16^{+2.09}_{-2.19}$, with a probability of 82% for this source of being a QSO. This is the source with the highest predicted photometric redshift of the sample. Since the Pan-STARRS counterpart is detected, even at such high redshift, a spectroscopic optical campaign is required to verify this prediction.

We found X-ray extended emission aligned with the radio jet structure in the northern side of our Chandra observation (see Figure 3, upper panel). The flux of of the X-ray counterpart is $(1.51 \pm 0.30) \times 10^{-14}$ erg cm^{-2} s^{-1} in the 0.5–7 keV band. Given the alignment with the jet rather than the lobe, the jet is most likely the source of the X-rays.

3.4. 3CR 390

3CR 390 is a lobe-dominated radio source, as shown in the VLA image at 4.5 GHz (see red/blue contours in the upper and lower panels of Figure 4 and the upper left panel of Figure A4). The IR counterpart of the radio core is detected in the WISE 3.4 μm filter image (see Figure 4, upper panel).

In the Pan-STARRS *R*-band image, there are both an optical source corresponding to the radio core, in the same position of the WISE counterpart, and an optical source located on the position of the western radio knot (see Figure 4, lower panel) that is likely to be a background source. To verify if the X-ray emission on the western side of the source is related to the diffuse radio emission or if it is an optical source, we measured the p-chance of the hotspot association considering the source density in a 80″ circular region around 3CR 390, taking into account the correct distance between the core and tentative hotspot. We obtained a p-chance <4%. As reported in Maselli et al. (2016), the whole radio structure is associated with NVSS J184537+095344 and the X-ray source: XRT J184537.6 +095349. The NVSS source, not well centered with respect to the 3CR positional uncertainty region, is located within the XRT positional uncertainty region. The infrared counterpart,

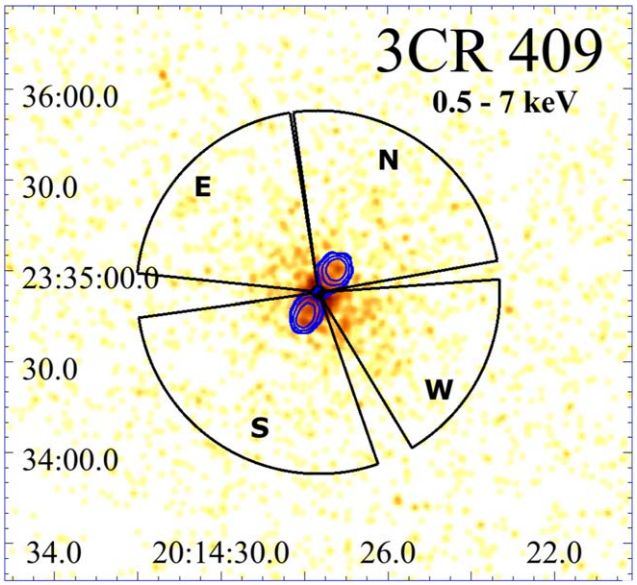

Figure 6. Directions used in source 3CR 409 to extract the surface brightness profiles shown in Figure 7. The four sectors extend up to 60″ from the core (that we have excluded, starting from a distance of 2″ from the position of the core, as reported in the NVSS; see Table 1). In blue we show the VLA contours from Figure 5.

namely, WISE J184537.60+095345.0, was also included in the all-sky catalog of blazar candidates by D'Abrusco et al. (2014) due to its peculiar infrared colors, and in D'Abrusco et al. (2019). Adopting the procedure described in Glowacki et al. (2017), using the 3.4 μm WISE magnitude, we obtained a photometric median redshift of $z = 0.41^{+0.28}_{-0.32}$, and using the 4.6 μm WISE magnitude a photometric median redshift of $z = 0.30^{+0.21}_{-0.25}$, with a probability of 57% for the source to be a QSO.

In the Chandra image the core is clearly detected and we also found extended X-ray emission spatially coincident with the radio bridge connecting the two intensity peaks visible at 4.5 GHz (see Figure 4, lower panel). Given the large number of X-ray photons measured within the 2″ circular region from the radio core position (i.e., above our threshold of 400 counts) we performed the X-ray spectral analysis. Adopting a power-law model with both Galactic and intrinsic absorption, we obtained the best-fit results, for both values of the photometric redshifts, setting $N_{\rm H,int}$ as a free parameter. In these cases, we obtain an $N_{\rm H,int}$ that is comparable with the Galactic $N_{\rm H}$ ($\sim 10^{21}$ cm^{-2}), and this result is not unexpected given that we were able to detect the optical counterpart in Pan-STARRS and the moderate z of 3CR 390.

3.5. 3CR 409

For 3CR 409, a lobe-dominated radio source, we merged two VLA observations, both at 1.4 GHz, obtained in different

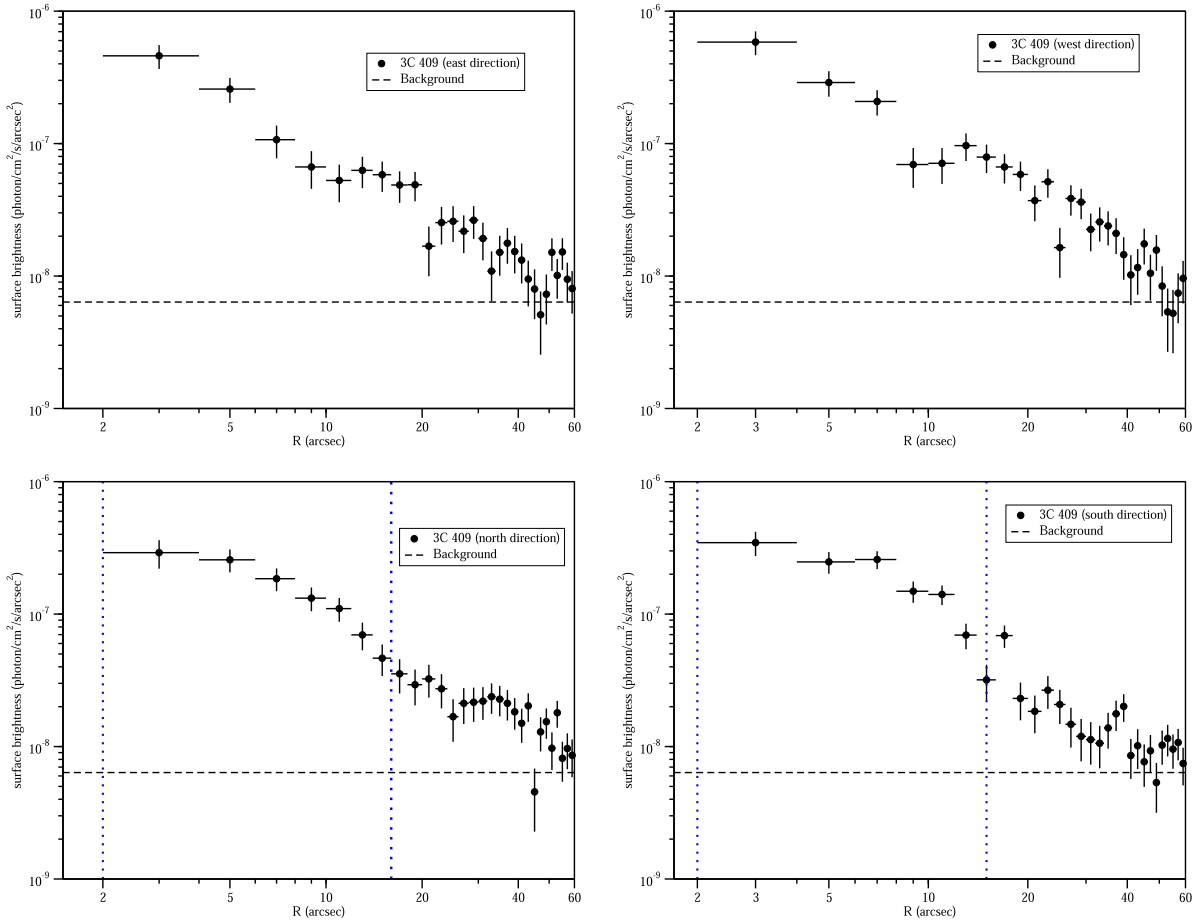

Figure 7. Surface brightness profiles for 3CR 409 extracted in the directions shown in Figure 6. Sectors are divided in bins of 2″ width. The inner and outer radii of the lobes are indicated with blue vertical dotted lines. In the western profile (upper right panel) we estimated a jump in the surface brightness between the third and fourth annulus, with 2.8σ.

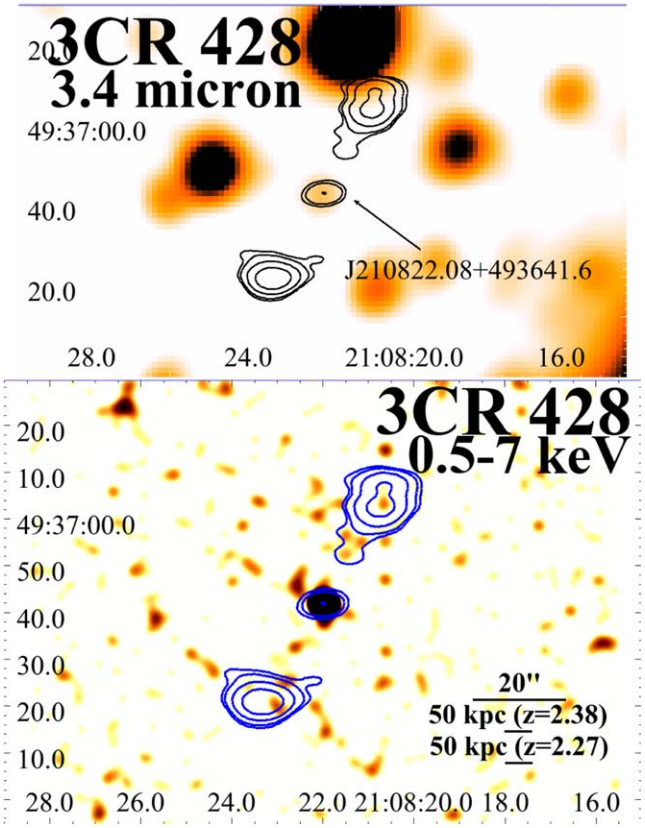

Figure 8. Upper panel: WISE 3.4 μm filter image of 3CR 428. VLA contours (black) at 4.5 GHz are the same used in the Chandra image (red). Radio contours start from 0.002 Jy beam^{-1} and increase by a factor of 2. The arrow points to the IR counterpart of the radio nucleus. No optical counterpart has been detected for this source. Lower panel: Chandra X-ray image of 3CR 428, filtered in the 0.5–7 keV band. Image has not been rebinned, but smoothed with a 6 pixel Gaussian kernel (equivalent to 2.″952). In the bottom right of the image, kiloparsec scales measured using the photometric redshifts obtained using the method described in Glowacki et al. (2017) are indicated.

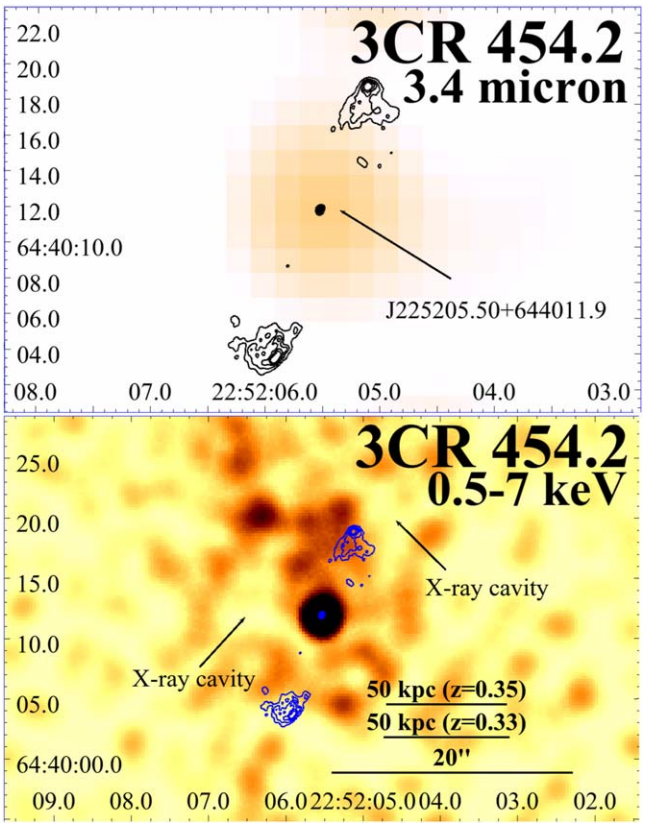

Figure 9. Upper panel: WISE 3.4 μm filter image of 3CR 454.2. VLA contours (black) are the same used in the Chandra image (blue) and start from 0.001 Jy beam^{-1} and increase by a factor of 0.001 Jy beam^{-1} to 0.005 Jy beam^{-1}. The arrow points to the IR counterpart of the radio nucleus. No optical counterpart has been detected for this source. Lower panel: Chandra X-ray image of 3CR 454.2, filtered in the 0.5–7 keV band, binned up to 0.″246 pixel^{-1} and smoothed with a 8 pixel Gaussian kernel (equivalent to 1.″968). Cavities are indicated by arrows. In the bottom right of the image, kiloparsec scales measured using the photometric redshifts obtained using the method described in Glowacki et al. (2017) are indicated.

configurations (see column (5) of Table 2 and black/blue contours in Figure 5). This is the only radio source of our sample to have been previously classified, as an FRII (Massaro et al. 2013). We manually flagged and calibrated both data sets separately, and then we performed the self-calibration of both observations together. In the final radio map (see Figure A5) the core is not clearly detected, and overlaying radio contours to the optical image we did not find a plausible counterpart located between the two lobes. On the other hand there is a WISE source, namely, J201427.59+233452.6, detected in all four filters and corresponding to the intensity peak of the Chandra image.

The source Swift J201427.5+233455, detected with S/N = 11.6, lies in the field of view of 3CR 409 and matches the coordinates of NVSS J201427+233452 with an angular separation of 1.″9. The mid-IR counterpart WISE J201427.59 +233452.6 is located at only 0.″3 from the NVSS source. This WISE infrared object is included in the all-sky catalog of blazar-like radio-loud sources by D'Abrusco et al. (2014) and in D'Abrusco et al. (2019). As for previous sources, adopting the procedure described in Glowacki et al. (2017), using the 3.4 μm WISE magnitude we obtained a median redshift of $z = 1.04^{+0.71}_{-0.74}$, and using the 4.6 μm WISE magnitude a median redshift of $z = 0.55^{+0.38}_{-0.46}$ and a probability of 60% of being a QSO.

In the Chandra image there is some extended emission around the core, suggesting the presence of a cluster, that we investigate in more detail. We have derived the surface brightness profiles in the directions shown in Figure 6. Northern and southern directions have been selected to encompass the radio lobe contours, while eastern and western directions are those away from the lobes. From these profiles we have estimated the extension of the diffuse emission that appears to be symmetrical around the source up to a distance of ∼60″ from the radio core. In the western direction, at a distance of ∼10″ there is a jump in the surface brightness, and the same behavior can be observed at the same distance in the eastern direction (see Figure 7).

Since we detected more than 400 photons in the nuclear region of the Chandra image, we also performed the spectral analysis of the X-ray core, adopting an absorbed power-law model. We obtained the best-fit results with $N_{\rm H,int}$ as a free parameter, for both choices of redshift. $N_{\rm H,int}$ has a value of $\sim 10^{23}$ cm^{-2}, and this is probably the reason we did not detect an optical counterpart, under the assumption of a normal gas to dust ratio.

We also analyzed the extended X-ray emission, adopting a thermal APEC model with Galactic absorption. As specified in Section 2.2.3, we have excluded a 2″ circular region where we

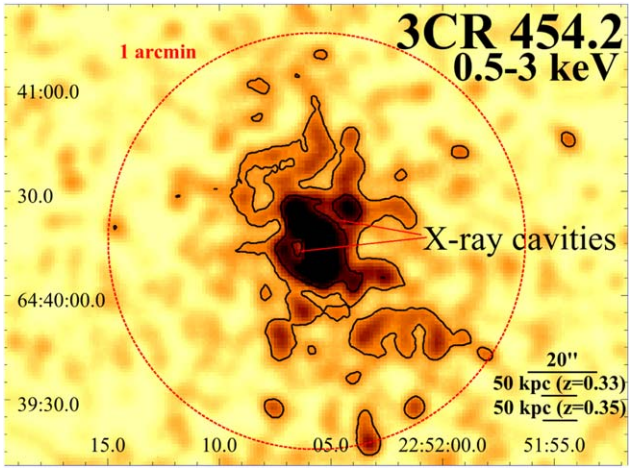

Figure 10. Chandra X-ray image of 3CR 454.2, filtered in the 0.5–3 keV band, binned up to 0.″984 pixel^{-1} and smoothed with a 4.″92 Gaussian kernel. The black circle has a 0.′5 radius. The black contours trace the X-ray emission at 0.1 and 0.2 counts pixel^{-1}. In the bottom right of the image, kiloparsec scales measured using the photometric redshifts obtained using the method described in Glowacki et al. (2017) are indicated.

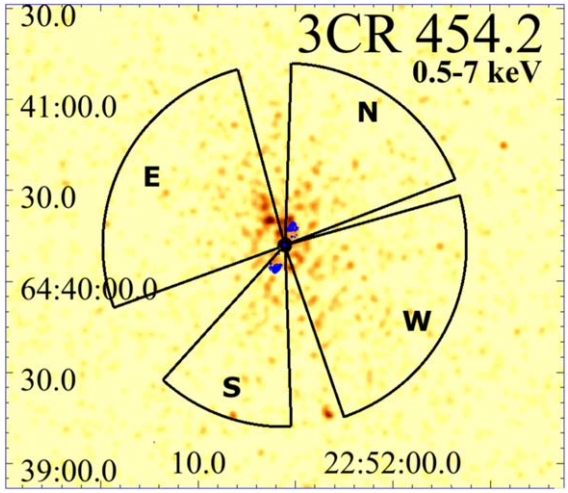

Figure 11. Directions used in source 3CR 454.2 to extract the surface brightness profiles shown in Figure 12. The four sectors extend up to 60″ from the core (that we have excluded, starting from a distance of 2″ from the position of the core, as reported in the NVSS; see Table 1). In blue we show the VLA contours from Figure 9.

expect to find most of the nuclear emission and all the detected point sources. However, we also took into account the contribution of Chandra's PSF wings extending into the region selected for the spectral extraction that accounts for about ∼2% of the 0.5–7 keV net counts. We therefore included such a contribution in the model used to fit the extended emission. We have tested four models: abundance fixed to 0.25 solar and redshift $z = 1.04$ (or $z = 0.55$), redshift $z = 1.04$ (or $z = 0.55$) and free abundance, abundance fixed to 0.25 solar and free redshift, and both abundance and redshift free to vary during the fit. The $z = 0.55$ models yield the best-fit statistics, with a poorly constrained temperature $\gtrsim$11 keV. Such temperatures have been reported for clusters at higher redshifts (e.g., $z = 0.89$; Jones et al. 2004), and therefore deeper Chandra observations are needed to draw firm conclusions on the nature of this extended X-ray emission.

3.6. 3CR 428

3CR 428 is a lobe-dominated radio source at 4.5 GHz with a clearly detected core (see black/red contours in Figure 8, upper and lower panels). There is no optical counterpart in the Pan-STARRS *R*-band image of the nucleus, while there is a detection at IR frequencies associated with WISE J210822.08 +493641.6 located within the XRT positional uncertainty region at an angular separation of 0.″5. The core is also clearly detected in the Chandra image, but there are no clear counterparts of radio lobes or hotspots. The X-ray source XRT J210822.1+493642 also matches the NVSS J210822 +493637 position at an angular separation of 5.″6.

As for 3CR 91, 3CR 390, and 3CR 409, the WISE counterpart has been recently included in the all-sky catalog of blazar candidates of D'Abrusco et al. (2014). Adopting the procedure described in Glowacki et al. (2017), using the 3.4 μm WISE magnitude we obtained a photometric redshift of $z = 2.38^{+1.62}_{-1.66}$, and using the 4.6 μm WISE magnitude a photometric redshift of $z = 2.27^{+1.59}_{-1.58}$, with a probability of 70% for the source being a QSO.

Since we detected more than 400 photons in the nuclear region of the Chandra image, we also performed a spectral analysis of the X-ray core, adopting an absorbed power-law model. As in the case of 3CR 409 we obtained a value of $N_{\rm H,int} \sim 10^{23}$ cm^{-2}, explaining our nondetection of an optical counterpart.

3.7. 3CR 454.2

3CR 454.2 is a lobe-dominated radio source in the 8 GHz VLA image, in which we clearly detected the core and two lobes and hotspots (see black contours in the upper panel of Figure 9). In the Pan-STARRS image there is no optical counterpart located at the radio core position.

In Maselli et al. (2016) a soft X-ray source XRT J225205.2 +644013 was detected, at an angular separation of 4.″6 from the coordinates of NVSS J225205+644010 within its 3CR positional uncertainty region. At an angular separation of 2.3″ from this NVSS source, the IR source WISE J225205.50 +644011.9 was also found in the AllWISE Catalogue, being its potential counterpart. It is well detected in all filters but the 22 μm filter. Adopting the procedure described in Glowacki et al. (2017), using the 3.4 μm WISE magnitude, we obtained a photometric redshift value of $z = 0.35^{+0.12}_{-0.11}$, and using the 4.6 μm WISE magnitude a value of $z = 0.33^{+0.12}_{-0.10}$, with a probability of 96% for the source of being an LERG.

In the Chandra image, we highlight the presence of extended X-ray emission and the possible presence of at least two cavities (reported in the lower panel of Figure 9 and, at a larger scale, in Figure 10). As in the case of 3CR 409 we have derived the surface brightness profiles in the directions shown in Figure 11. Again, northern and southern directions have been selected to encompass the radio lobes contours, while eastern and western directions are those away from the lobes. We found evidence for diffuse emission up to ∼50″ from the core (see Figure 12). The northwestern cavity has less than 2σ level significance, while the southeastern one has a significance of 3.4σ. To evaluate the significance of the cavities, we have estimated the counts in each cavity, using circular regions of appropriate radii, and the average level of the diffuse emission at the same distance from the core using several circular regions with the same radii of the cavity regions. Then, using Poisson statistics, we evaluated the Gaussian σ equivalent of the cavities significance. We have performed a spectral analysis

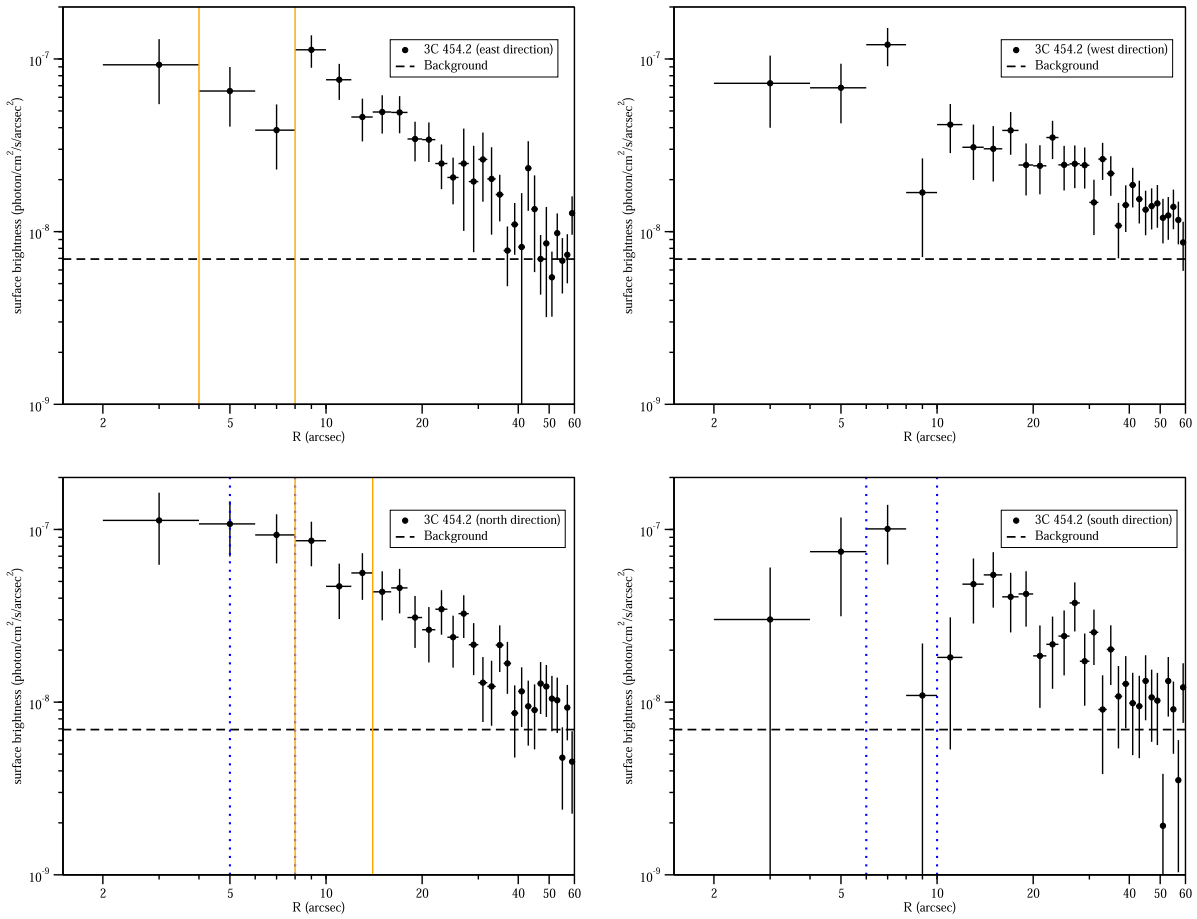

Figure 12. Surface brightness profiles for 3CR 454.2 extracted in the directions shown in Figure 11. Sectors are divided in bins of 2″ width. In the northern and southern profiles (bottom panels of Figure 12) inner and outer radii of the lobes are indicated with blue vertical dotted lines. In the northern and eastern profiles the areas occupied by the cavities are included between orange vertical lines.

of the diffuse X-ray emission, adopting a thermal model, in every possible combination of redshift and abundance values, fixed or free. As specified in Section 2.2.3, we have excluded a 2″ circular region including the nuclear emission, but since the contribution of the wings of the PSF was lower than 1%, we have excluded this contribution in the thermal model of the extended emission. Due to low count statistics, all fits are poorly constrained and the uncertainties on the temperature are large. Also in this case, deeper Chandra observations are needed to properly constrain the properties of the cluster IGM.

4. Summary and Conclusions

In this paper, we present a multiwavelength (radio, infrared, optical, and X-ray) study of 7 of the 25 extragalactic radio sources listed in the Third Cambridge Revised Catalog (3CR) as unidentified by Spinrad et al. (1985). All these sources, previously, lacked a confirmed optical counterpart and thus miss redshift and optical classification. The 3CR Chandra Snapshot Survey, started in 2008, aimed at searching for X-ray emission from jet knots, hotspots, and lobes, studying the nuclear emission of their host galaxies and investigating their environments at all scales.

Adopting the same procedures used in the previous papers of the Snapshot, we can summarize our results as follows:

1. Six of the seven sources (all but 3CR 409), show a clear detection of the radio core at 1.5 GHz, 6 GHz, and 10 GHz. These radio images, retrieved from the historical VLA archive, were all manually reduced and for five sources we also gave a tentative FRII radio classification.
2. We found IR counterparts to all the radio cores, thanks to the WISE archival images. This allowed us to estimate the photometric redshift of the counterparts using the magnitudes at 3.4 and 4.6 μm as described in Glowacki et al. (2017). This method allowed us also to give tentative classifications (LERG/HERG/QSO) of the sources in the sample. Most of the sources are classified as QSOs with a probability $\gtrsim$60% , while 3CR 131 and 3CR 454.2 are classified as LERGs, with the same probability.
3. Only three sources (namely, 3CR 91, 3CR 158, and 3CR 390) of the seven with an infrared counterpart are also detected in the optical band using Pan-STARRS images. For the other sources we have obtained an $N_{\rm H,int}$ value of the order of $\sim 10^{23}$ cm^{-2}, and corresponding levels of dust obscuration are likely the reason for the nondetection of the optical counterpart.
4. We found Chandra X-ray counterparts for all the radio cores. Then, for 3CR 91, 3CR 390, 3CR 490, and 3CR 428, we also estimated the X-ray spectral indices ($\alpha_{\rm X} = 0.48$–0.80) and the intrinsic absorption $N_{\rm H,int}$, via spectral analysis. The

spectral indices are compatible with results reported in the literature for the nuclei of QSOs and LERGs.
5. We detected X-ray emission arising from the X-ray counterpart of the northern radio jet in 3CR 158 as well as that associated with the radio bridge in 3CR 390.
6. Our Chandra observations also revealed the presence of extended X-ray emission, the hallmark of galaxy clusters, around 3CR 409 and 3CR 454.2. We performed a spectral analysis, but temperature or spectral parameters are unconstrained. This demands deeper Chandra observations to make more conclusive measures of the temperature, mass, and luminosity of the clusters.

Regarding the tentative classification of the sources in our sample, our results are:

1. 3CR 91 has an 8 GHz radio structure similar to an FRII radio galaxy. From the WISE magnitudes of the counterpart it can be classified as a QSO at $z \sim 0.2$. The Pan-STARRS core counterpart is detected, and the intrinsic absorption value estimated from X-ray spectral fitting is of the same order of magnitude as the Galactic one. We therefore classify this source as a QSO at $z \sim 0.2$.
2. 3CR 131 has an 8 GHz radio structure similar to an FRII radio galaxy. From the WISE magnitudes of the counterpart, it can be classified as an LERG at $z \sim 0.4$. There is no Pan-STARRS detected counterpart, but there are not enough nuclear counts in the Chandra image to perform a spectral analysis. We classify this source as an FRII–LERG at $z \sim 0.4$.
3. 3CR 158, at 8 GHz, is similar to an FRII, and we detected X-ray extended emission aligned with the radio jet structure. The photometric redshift estimate from WISE magnitudes is $z \sim 4$, and the source is classified as a QSO. The poor statistics do not allow us to perform a spectral analysis of the source nucleus. The Pan-STARRS core counterpart is detected with $m_R = 20.6$, the highest of the sample. From these results, we classify this source as a high-redshift ($\gtrsim$4) QSO.
4. 3CR 390 does not have a clear radio morphology, showing two-sided lobes. From the WISE magnitudes of the counterpart, this source can be classified as a QSO at $z \sim 0.4$. This source has a detected Pan-STARRS nuclear counterpart, and from the X-ray spectral fitting, we estimate a nuclear intrinsic absorption comparable to the Galactic one. We classify this source as a QSO at $z \sim 0.4$.
5. 3CR 409 shows an FRII radio morphology, and from the WISE magnitudes this source is classified as a QSO at $z \sim 0.9$. This source appears to lie in a cluster of galaxies, and does not have a detected Pan-STARRS nuclear counterpart. From the X-ray spectral fitting, we estimate an intrinsic absorption $\sim 10^{23}$ cm^{-2}. We therefore classify this source as a highly absorbed QSO at $z \sim 0.9$.
6. 3CR 428 features an FRII-like radio morphology. The WISE magnitudes of this source classify it as a QSO at $z \sim 2.3$. No Pan-STARRS nuclear counterpart is detected, and from the X-ray spectral fit we estimate an intrinsic absorption $\sim 10^{23}$ cm^{-2}. We classify this source as a highly absorbed QSO at $z \sim 2.3$.
7. 3CR 454.2 features an FRII-like radio morphology. From the WISE magnitudes we classify this source as an LERG at $z \sim 0.3$. We do not detect a nuclear Pan-STARRS counterpart. This source appears to lie in a galaxy cluster with disturbed IGM morphology; however, the available Chandra data do not allow nuclear spectral analysis and so no estimate of the intrinsic absorption, or the IGM temperature. Deeper X-ray observations are needed to draw firm conclusions on this source.

In conclusion, we have four sources with a predicted low-z host ($z \sim 0.2$–0.4), namely, 3CR 91, 3CR 131, 3CR 390, and 3CR 454.2. Three sources are classified as high-z ($>$0.9), highly absorbed QSOs, namely, 3CR 158, 3CR 409, and 3CR 428. In the case of 3CR 158, since the estimated photometric redshift is that of a very high-z source, deeper Chandra observations are required to verify this estimate.

This paper presents the first attempt to describe in more detail the unidentified sources in the 3CR Catalog, using new Chandra X-ray observations and archival observations from VLA, WISE, and Pan-STARRS observatories, leading to the discovery of X-ray emission from nuclei, jets, and cluster gas. This last part of the 3CR Snapshot Survey, devoted to the 3CR unidentified sources, is still ongoing and we expect to close this exploratory sample of nine sources–awarded in Chandra observation Cycle 21–around 2021 April, with additional sources scheduled for the rest of the year.

Dan Harris passed away 2015 December 6. His career spanned much of the history of radio and X-ray astronomy. His passion, insight, and contributions will always be remembered. A significant fraction of this work is one of his last efforts. We thank the referee for a careful reading of our manuscript and many helpful comments that led to improvements in the paper. This work is supported by the "Departments of Excellence 2018-2022" Grant awarded by the Italian Ministry of Education, University and Research (MIUR) (L. 232/2016). This research has made use of resources provided by the Ministry of Education, Universities and Research for the grant MASF_FFABR_17_01. This investigation is supported by the National Aeronautics and Space Administration (NASA) grants GO9-20083X and GO0-21110X. A.P. acknowledges financial support from the Consorzio Interuniversitario per la fisica Spaziale (CIFS) under the agreement related to the grant MASF_CONTR_FIN_18_02. A.J. acknowledges the financial support (MASF_CONTR_FIN_18_01) from the Italian National Institute of Astrophysics under the agreement with the Instituto de Astrofisica de Canarias for the "Becas Internacionales para Licenciados y/o Graduados Convocatoria de 2017." W.F. and R.K. acknowledge support from the Smithsonian Institution and the Chandra High Resolution Camera Project through NASA contract NAS8-03060. C.S. acknowledges support from the ERC-StG DRANOEL, No. 714245. The National Radio Astronomy Observatory is operated by Associated Universities, Inc., under contract with the National Science Foundation. This research has made use of data obtained from the High-Energy Astrophysics Science Archive Research Center (HEASARC) provided by NASA's Goddard Space Flight Center; the SIMBAD database operated at CDS, Strasbourg, France; the NASA/IPAC Extragalactic Database (NED) operated by the Jet Propulsion Laboratory, California Institute of Technology, under contract with the National Aeronautics and Space Administration. This publication makes use of data products from the Wide-field Infrared Survey Explorer, which is a joint project of the University of California, Los Angeles, and the Jet Propulsion Laboratory/California Institute of Technology, funded by the National

Aeronautics and Space Administration. This research has made use of data obtained from the Chandra Data Archive. The Pan-STARRS1 Surveys (PS1) and the PS1 public science archive have been made possible through contributions by the Institute for Astronomy, the University of Hawaii, the Pan-STARRS Project Office, the Max-Planck Society and its participating institutes, the Max Planck Institute for Astronomy, Heidelberg and the Max Planck Institute for Extraterrestrial Physics, Garching, The Johns Hopkins University, Durham University, the University of Edinburgh, the Queen's University Belfast, the Harvard-Smithsonian Center for Astrophysics, the Las Cumbres Observatory Global Telescope Network Incorporated, the National Central University of Taiwan, the Space Telescope Science Institute, the National Aeronautics and Space Administration under grant No. NNX08AR22G issued through the Planetary Science Division of the NASA Science Mission Directorate, the National Science Foundation grant No. AST-1238877, the University of Maryland, Eotvos Lorand University (ELTE), the Los Alamos National Laboratory, and the Gordon and Betty Moore Foundation. This research has made use of software provided by the Chandra X-ray Center (CXC) in the application packages CIAO, and Sherpa. TOPCAT (http://www.star.bris.ac.uk/~mbt/topcat/; Taylor 2005) was used for the preparation and manipulation of the tabular data. SAOImage DS9 and CASA were used extensively in this work for the preparation and manipulation of the images. SAOImage DS9 was developed by the Smithsonian Astrophysical Observatory.

Facility: VLA, CXO (ACIS), WISE, Pan-STARRS.

Appendix
Radio Contours of the Sources and Tables

For all the 3CR sources in our sample, radio contours are shown here in Figures A1–A7. For each source, we have specified the band and configuration at which the observation was performed: *L* band (1.5 GHz), *C* band (6 GHz), and *X* band (10 GHz), in A (maximum baseline, $B_{\rm max}$, equal to 35 km), B ($B_{\rm max} = 10$ km), C ($B_{\rm max} = 3.5$ km), or D ($B_{\rm max} = 1$ km) configuration. In the bottom left corner, the clean beam is shown as a black filled ellipse. In Table 1 a summary of X-ray observations is reported. All the details about the single radio observations are reported in Table 2. In Table 3 a summary of optical and IR observations is reported. In Table 4 we report X-ray fluxes for the cores. In Table 5 we report the results of the spectral analysis performed on the four sources with cores with more than 400 photons detected.

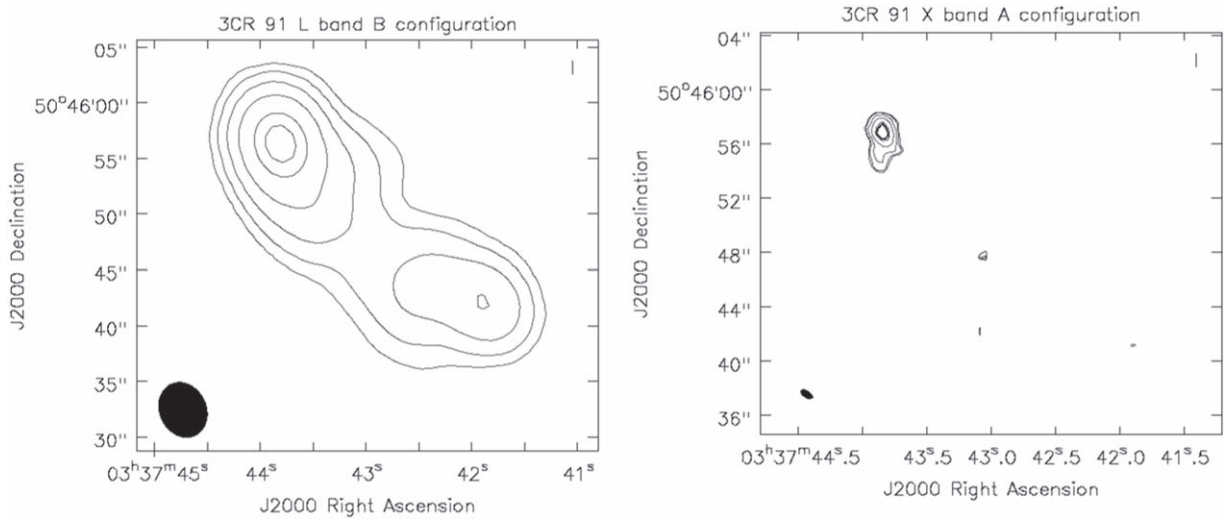

Figure A1. Radio VLA contours of 3CR 91. The name of the source, the observing band, and array configuration are reported at the top of each panel. The clean beam is shown as a black filled ellipse in the bottom left of the image. Radio contours are reported in the last column in Table 2. At the top of each panel, name, band, and configuration are reported.

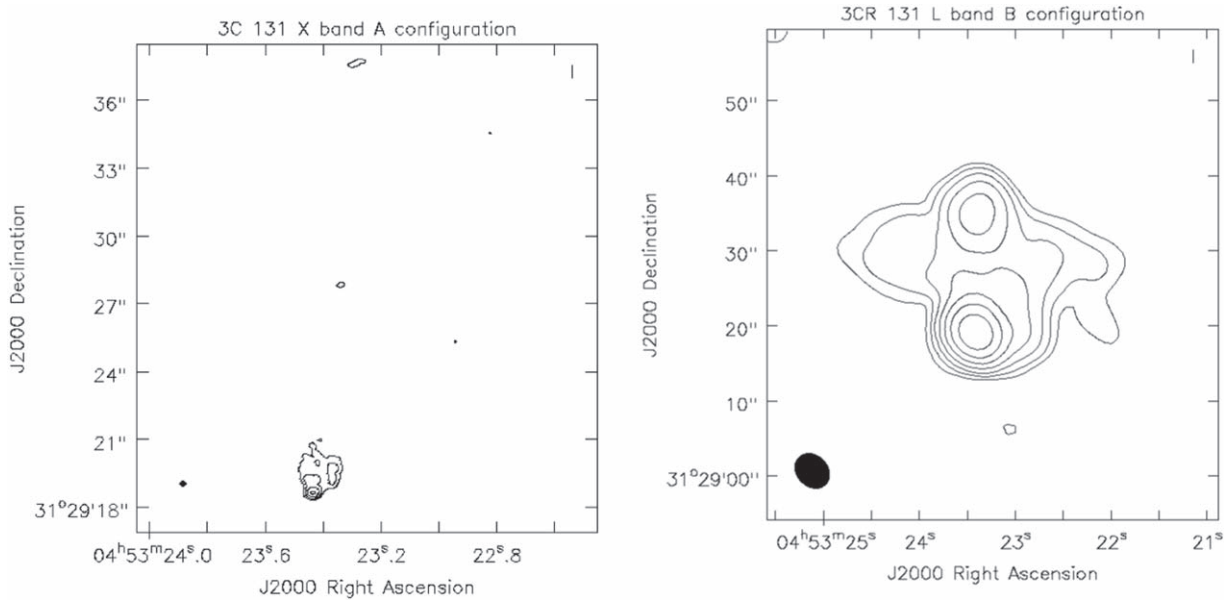

Figure A2. Radio VLA contours of 3CR 131. The name of the source, the observing band, and array configuration are reported at the top of each panel. The clean beam is shown as a black filled ellipse in the bottom left of the image. Radio contours are reported in the last column in Table 2.

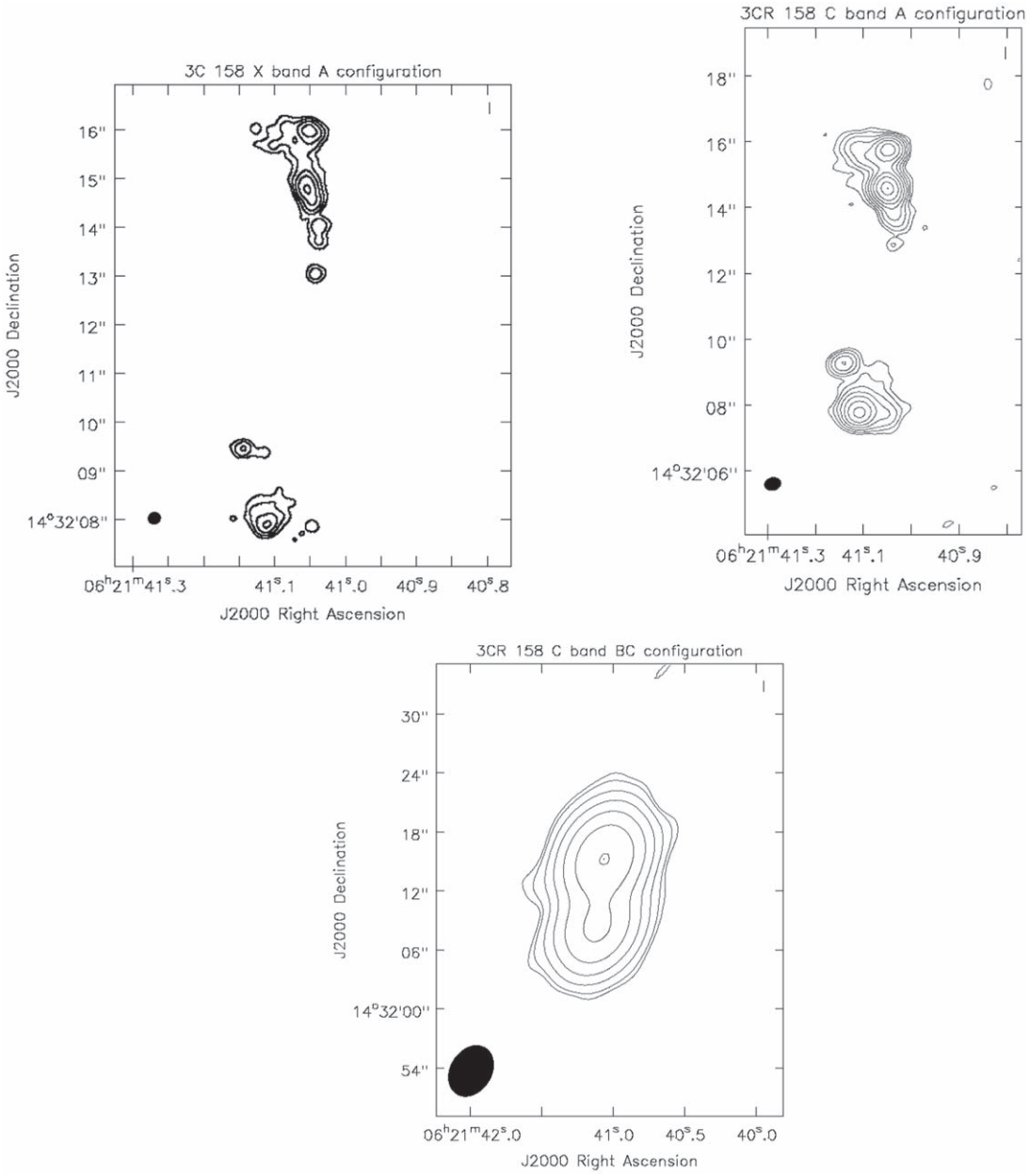

Figure A3. Radio VLA contours of 3CR 158. The name of the source, the observing band, and array configuration are reported at the top of each panel. The clean beam is shown as a black filled ellipse in the bottom left of the image. Radio contours are reported in the last column in Table 2.

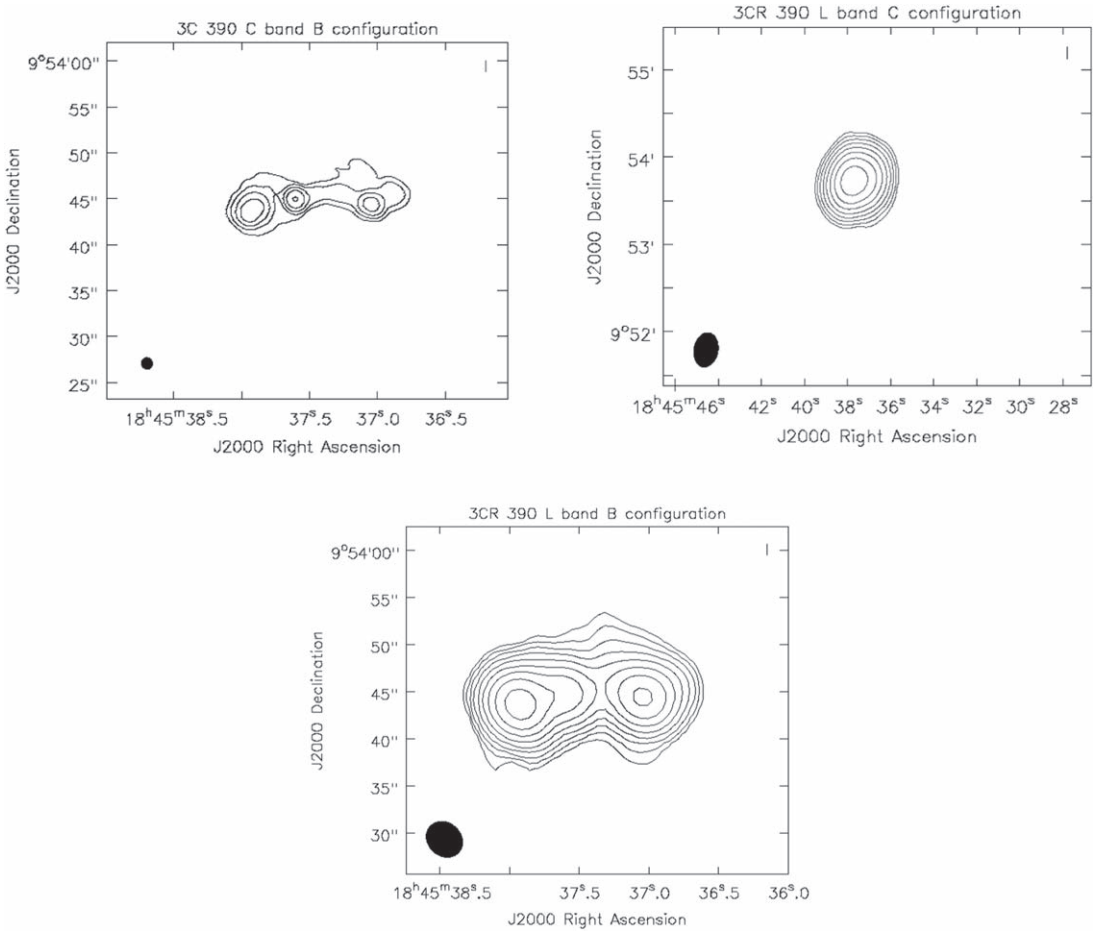

Figure A4. Radio VLA contours of 3CR 390. The name of the source, the observing band, and array configuration are reported at the top of each panel. The clean beam is shown as a black filled ellipse in the bottom left of the image. Radio contours are reported in the last column in Table 2.

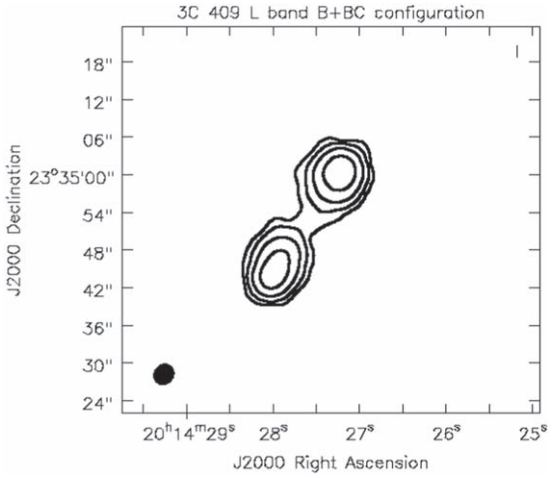

Figure A5. Radio VLA contours of 3CR 409. This map has been obtained merging two observations in B and BC configurations, respectively, as described in Section 3. The name of the source, the observing band, and array configuration are reported at the top of each panel. The clean beam is shown as a black filled ellipse in the bottom left of the image. Radio contours are reported in the last column in Table 2.

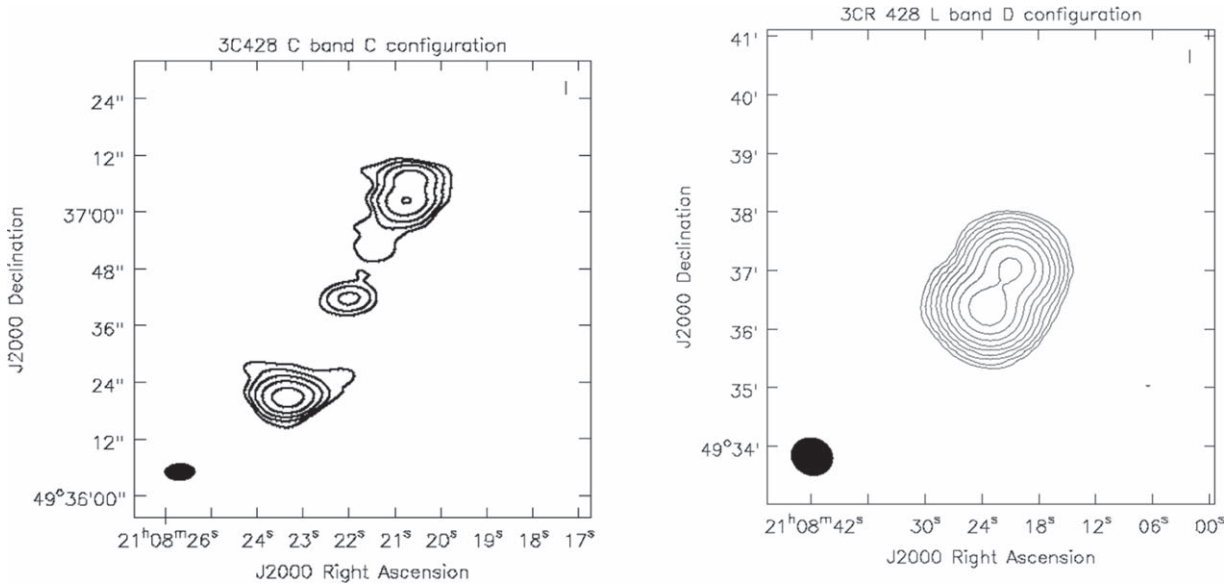

Figure A6. Radio VLA contours of 3CR 428. The name of the source, the observing band, and array configuration are reported at the top of each panel. The clean beam is shown as a black filled ellipse in the bottom left of the image. Radio contours are reported in the last column in Table 2.

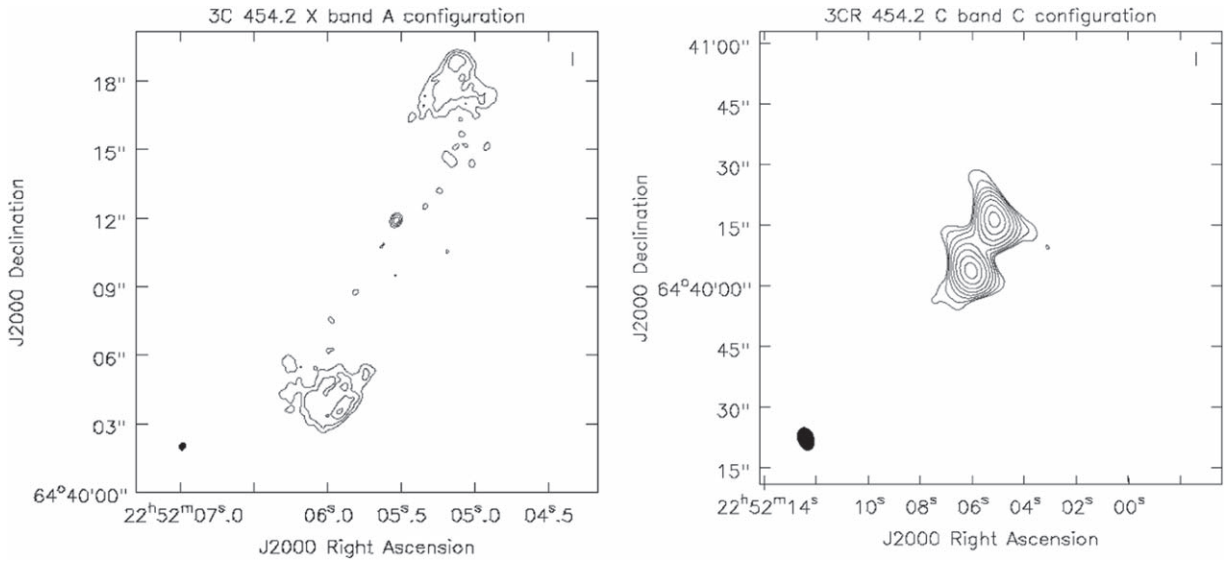

Figure A7. Radio VLA contours of 3CR 454.2. The name of the source, the observing band, and array configuration are reported at the top of each panel. The clean beam is shown as a black filled ellipse in the bottom left of the image. Radio contours are reported in the last column in Table 2.

Table 1
Summary of X-Ray Observations

3CR Name	R.A. (J2000) (hh mm ss)	Decl. (J2000) (dd mm ss)	$N_{H,Gal}$ (10^{21} cm^{-2})	Chandra Obs. ID	Obs. Date (yyyy-mm-dd)	Exposure (ks)	S_{178} (Jy)	Counterpart	Radio Nucleus	Cluster
(1)	(2)	(3)	(4)	(5)	(6)	(7)	(8)	(9)	(10)	(11)
91	03 37 43.032	+50 45 47.622	4.88	22626	2019-11-18	18.9	14.1	IR, opt	yes	no
131	04 53 23.337	+31 29 27.826	2.36	22627	2019-12-29	23.8	14.6	IR	yes	no
158	06 21 41.041	+14 32 13.035	4.95	22629	2020-01-10	23.75	18.1	IR, opt	yes	no
390	18 45 37.601	+09 53 44.998	3.00	22630	2020-02-28	19.8	21.0	IR, opt	yes	no
409	20 14 27.74*	+23 34 58.4*	2.49	22631	2019-11-29	19.81	76.6	IR	no	yes
428	21 08 21.985	+49 36 41.820	10.9	22632	2019-12-23	20.79	16.6	IR	yes	no
454.2	22 52 05.530	+64 40 11.940	7.48	22633	2019-11-17	19.8	8.8	IR	yes	yes

Note. Column (1): the 3CR name. Columns (2)–(3): the celestial positions obtained from the radio images (the only exception is 3CR 409 where we used the NVSS counterpart coordinates). Column (4): Galactic neutral hydrogen column densities $N_{H,Gal}$ along the line of sight (Kalberla et al. 2005). Column (5): the Chandra observation ID. Column (6): the date when the Chandra observation was performed. Column (7): exposure time in ks, as reported in the Chandra Archive. Column (8): S_{178} is the flux density at 178 MHz, from Spinrad et al. (1985). Columns (9)–(11): remarks on the results of this work.

Table 2
Summary of Radio Observations

3CR Name	NRAO ID	Obs. Date (yyyy-mm-dd)	Frequency (GHz)	Configuration	Beam Size ($arcsec^2$)	Total Flux (Jy)	Peak Flux (Jy $beam^{-1}$)	TOS (s)	rms (σ) (10^{-3} Jy $beam^{-1}$)	Contour Levels (σ)
(1)	(2)	(3)	(4)	(5)	(6)	(7)	(8)	(9)	(10)	(11)
91	AH976	2008-10-09	8.44, 8.49	AB	1×0.5	0.63 ± 0.06	4.25×10^{-2}	70	1.4	6, 8, 16, 32, 64, 72, 74, 78
⋯	AP001	1986-09-15	1.45	B	5.1×4.2	3.39 ± 0.17	1.43	150	1.23	9, 27, 81, 243, 729, 1162
131	AH976	2008-10-09	8.44, 8.49	A	0.28×0.22	0.36 ± 0.04	1.28	70	0.33	5, 20, 80, 320, 1280, 5120
⋯	AP001	1986-09-15	1.45	B	7×6	2.8 ± 0.14	1.3	150	2.8	4, 8, 16, 32, 64, 128, 256, 512
158	AH976	2008-10-09	8.44, 8.49	A	0.22×0.20	0.63 ± 0.03	1.28×10^{-1}	70	0.44	3, 9, 27, 81, 243
⋯	AR069	1983-10-13	4.84, 4.89	A	0.5×0.4	0.58 ± 0.03	1.57×10^{-1}	260	0.29	3, 6, 12, 24, 48, 96, 192, 384, 548
⋯	AF156	1989-07-21	4.84, 4.89	BC	5.52×4.17	0.58 ± 0.03	3.93×10^{-1}	310	0.17	5, 9, 27, 81, 243, 729, 2187, 2258
390	AT147	1993-03-24	4.84, 4.89	B	1.3×1.2	1.17 ± 0.06	3.04×10^{-1}	370	0.10	10, 40, 160, 640, 2560
⋯	AK100	1984-02-27	1.41, 1.64	B	4.1×3.5	4.42 ± 0.22	2.145	400	0.69	8, 16, 32, 64, 128, 256, 512, 1024, 2048, 3110
⋯	AP001	1986-11-28	1.45	C	23.9×16.6	4.6 ± 0.23	2.4×10^{-1}	210	2.8	6, 12, 24, 48, 96, 192, 384, 768, 1536
409	AP001	1986-09-15	1.45	BC	3.5×3.1	12.54 ± 0.63	2.06×10^{-1}	190	4	5, 20, 80, 320, 1280
⋯	AC169	1986-08-09	1.39, 1.42, 1.46, 1.51, 1.63, 1.66	B	⋯	⋯	⋯	980	⋯	⋯
428	AF102	1985-07-30	4.84, 4.89	C	6.4×3.5	0.51 ± 0.02	2.06	300	0.26	2, 4, 8, 16, 32, 64, 128, 512, 1024, 8000
⋯	AH147	1984-09-19	1.45, 1.5	D	43.2×38	2.16 ± 0.11	1.17	4680	0.45	6, 12, 24, 48, 96, 192, 384, 768, 1536, 3072
454.2	AH976	2008-10-09	8.44, 8.49	A	0.34×0.28	0.25 ± 0.02	1.11×10^{-2}	80	0.29	3, 6, 12, 24, 38
⋯	AS238	1985-07-14	4.84, 4.89	C	5.7 x 4	0.66 ± 0.03	1.82×10^{-1}	270	0.27	6, 12, 24, 48, 96, 192, 384, 674

Note. Column (1): the 3CR name. Column (2): the NRAO observing project (or proposal) identification. Column (3): date of the observation. Column (4): frequency of the VLA observation. Column (5): array configuration. Column (6): size of the elliptical clean beam (major axis × minor axis). Column (7): total flux of the source, as obtained from the self-calibration. Column (8): peak flux of the radio image. Column (9): observation time on source (TOS). Column (10): rms noise of the clean image. Column (11): contour levels in units of rms.

Table 3
Summary of Optical and IR Observations

3CR Name	NVSS Name	WISE Name	$E(B-V)$ (mag)	w1 (mag)	w2 (mag)	w3 (mag)	R Band (mag)	z_{w1}	z_{w2}	VLA/Chandra (arcsec)
(1)	(2)	(3)	(4)	(5)	(6)	(7)	(8)	(9)	(10)	(11)
91	J033743+504552	J033743.02+504547.6	1.05 ± 0.05	11.885 ± 0.022	10.80 ± 0.021	7.936 ± 0.020	20.29 ± 0.05	0.23 ± 0.18	$0.19^{+0.18}_{-0.14}$	0.43
131	J045323+312924	J045323.34+312928.4	0.83 ± 0.02	14.98 ± 0.041	14.77 ± 0.082	12.306	⋯	$0.41^{+0.13}_{-0.12}$	0.44 ± 0.13	0.65
158	J062141+143211	J062141.01+143212.8	0.77 ± 0.02	15.133 ± 0.046	13.953 ± 0.043	11.131 ± 0.189	20.62 ± 0.06	$4.57^{+0.68}_{-3.14}$	$3.16^{+2.09}_{-2.19}$	0.35
390	J184537+09534	J184537.60+095345.0	0.49 ± 0.01	12.546 ± 0.043	11.575 ± 0.024	9.150 ± 0.029	18.80 ± 0.06	$0.41^{+0.28}_{-0.32}$	$0.30^{+0.21}_{-0.25}$	0.02
409	J201427+233452	J201427.59+233452.6	0.57 ± 0.03	13.547 ± 0.050	12.377 ± 0.027	9.005 ± 0.027	⋯	$1.04^{+0.71}_{-0.74}$	$0.55^{+0.38}_{-0.46}$	…[a]
428	J210822+493637	J210822.08+493641.6	2.59 ± 0.07	14.559 ± 0.064	13.097 ± 0.035	10.143 ± 0.056	⋯	$2.38^{+1.62}_{-1.66}$	$2.27^{+1.59}_{-1.58}$	1.09
454.2	J225205+644010	J225205.50+644011.9	1.26 ± 0.04	14.652 ± 0.030	14.341 ± 0.042	13.121 ± 0.467	⋯	$0.35^{+0.12}_{-0.11}$	$0.33^{+0.12}_{-0.10}$	0.72

Notes. Column (1): the 3CR name. Column (2): associated NVSS source. Column (3): associated WISE source. Column (4): extinction, as reported in the NASA/IPAC Infrared Science Archive (IRSA). Column (5): magnitude in the WISE w1 filter (3.4 μm). Column (6): magnitude in the WISE w2 filter (4.6 μm). Column (7): magnitude in the WISE w3 filter (12 μm). Column (8): magnitude in the Pan-STARRS R band. Column (9): median redshift value obtained from 3.4 μm filter magnitude. Column (10): median redshift value obtained from 4.6 μm filter magnitude. Column (11): angular separation between the position of the radio core detected in the VLA maps and that of the associated X-ray counterpart in the Chandra images (see Section 2.2). For the estimate of the photometric redshift we have used dereddened values of the WISE magnitude corrected for Galactic absorption using reddening estimates from Schlafly & Finkbeiner (2011) and the extinction model from Fitzpatrick & Massa (2007).

[a] Since we were unable to detect the position of the radio core of 3CR409, the Swift is missing.

Table 4
X-Ray Emission From Nuclei

3CR Name (1)	Net Counts (2)	$F^*_{0.5-1\,\mathrm{keV}}$ (cgs) (3)	$F^*_{1-2\,\mathrm{keV}}$ (cgs) (4)	$F^*_{2-7\,\mathrm{keV}}$ (cgs) (5)	$F^*_{0.5-7\,\mathrm{keV}}$ (cgs) (6)
91	1938.5 (44.0)	2.5 (0.5)	21.5 (0.8)	92.4 (2.7)	116.4 (2.8)
131	62.4 (8.0)	⋯	0.2 (0.1)	3.8 (0.5)	3.9 (0.5)
158	288.4 (17.0)	0.5 (0.2)	2.8 (0.3)	9.2 (0.7)	12.5 (0.8)
390	1068.5 (32.7)	4.1(0.6)	12.7 (0.6)	40.2 (1.7)	57.0 (1.9)
409	596.5 (24.4)	0.3 (0.2)	3.6 (0.3)	35.3 (1.6)	39.2 (1.7)
428	557.5 (23.6)	0.2 (0.1)	3.9 (0.3)	28.5 (1.4)	32.6 (1.4)
454.2	33.5 (5.8)	⋯	0.1 (0.1)	2.1 (0.4)	2.2 (0.4)

Note. Column (1): 3CR name. Column (2): background-subtracted number of photons within a circle of radius $r = 2''$ in the 0.5–7 keV band. Column (3): measured X-ray flux between 0.5 and 1 keV. Column (4): measured X-ray flux between 1 and 2 keV. Column (5): measured X-ray flux between 2 and 7 keV. Column (6): measured X-ray flux between 0.5 and 7 keV. Note: (*) fluxes are given in units of 10^{-14} erg cm^{-2} s^{-1} and 1σ uncertainties in the number of photons computed assuming Poisson statistics are given in parentheses. The uncertainties on the flux measurements are computed as described in Section 2. Fluxes were not corrected for Galactic absorption and were computed adopting the same X-ray photometric measurements of Massaro et al. (2015).

Table 5
Results of Nuclear X-Ray Spectral Analysis

3CR Name (1)	z (2)	$N_{\mathrm{H,int}}$ (10^{22} cm^{-2}) (3)	α_{X} (4)	ν (5)	χ^2_ν (6)	Luminosity (erg s^{-1}) (7)
91	0.23	$0.33^{+0.25}_{-0.23}$	0.8*	25	0.91	$1.37^{+0.12}_{-0.11} \times 10^{44}$
91	0.23	0*	0.50 ± 0.12	25	0.77	$1.23^{+0.22}_{+0.18} \times 10^{44}$
91	0.19	$0.31^{+0.23}_{-0.21}$	0.8*	25	0.91	$8.87^{+0.72}_{-0.78} \times 10^{43}$
91	0.19	0*	0.50 ± 0.12	25	0.77	$8.07^{+1.50}_{-1.22} \times 10^{43}$
390	0.41	$0.50^{+0.18}_{-0.20}$	0.8*	45	0.86	$6.03^{+0.40}_{-0.33} \times 10^{44}$
390	0.41	0*	0.50 ± 0.08	45	0.75	$5.45^{+0.60}_{-0.62} \times 10^{44}$
390	0.30	$0.40^{+0.16}_{-0.15}$	0.8*	45	0.86	$2.89^{+0.18}_{-0.17} \times 10^{44}$
390	0.30	0*	0.50 ± 0.08	45	0.75	$2.62^{+0.27}_{-0.25} \times 10^{44}$
409	1.04	$14.4^{+1.74}_{-1.56}$	0.8*	25	0.71	$7.51^{+0.65}_{-0.53} \times 10^{45}$
409	1.04	$11.19^{+3.00}_{-2.77}$	$0.45^{+0.28}_{-0.27}$	24	0.68	$6.22^{+3.28}_{-2.71} \times 10^{45}$
409	0.55	$6.80^{+0.76}_{-0.70}$	0.8*	25	0.68	$1.40^{+0.10}_{-0.11} \times 10^{45}$
409	0.55	$5.66^{+1.51}_{-1.41}$	$0.53^{+0.31}_{-0.30}$	24	0.68	$1.21^{+0.64}_{-0.52} \times 10^{45}$
428	2.38	$23.37^{+5.96}_{-5.64}$	0.8*	23	0.64	$4.32^{+0.40}_{-0.39} \times 10^{46}$
428	2.38	$19.89^{+16.65}_{-14.81}$	$0.71^{+0.38}_{-0.36}$	22	0.67	$4.09^{+2.66}_{-2.14} \times 10^{46}$
428	2.27	$21.49^{+5.52}_{-5.20}$	0.8*	23	0.63	$3.86^{+0.34}_{0.34} \times 10^{46}$
428	2.27	$18.37^{+14.92}_{-13.16}$	$0.71^{+0.36}_{-0.34}$	22	0.66	$3.71^{+2.49}_{-1.94} \times 10^{46}$

Note. Column (1): the 3CR name. Column (2): photometric redshifts, obtained from WISE magnitudes in 3.4 and 4.6 μm filters as described in the text, used for the spectral analysis. Column (3): intrinsic absorption, $N_{\mathrm{H,int}}$, as used in the spectral model. Column (4): X-ray spectral index. Column (5): degree of freedom. Column (6): reduced statistic. Column (7): luminosity of the nucleus, obtained in SHERPA with the function sample_flux. Parameters fixed in the spectral fitting are indicated with an asterisk (*).

ORCID iDs

V. Missaglia https://orcid.org/0000-0001-8382-3229
F. Massaro https://orcid.org/0000-0002-1704-9850
A. Paggi https://orcid.org/0000-0002-5646-2410
R. P. Kraft https://orcid.org/0000-0002-0765-0511
W. R. Forman https://orcid.org/0000-0002-9478-1682
A. Jimenez-Gallardo https://orcid.org/0000-0003-4413-7722
F. Ricci https://orcid.org/0000-0001-5742-5980
C. Stuardi https://orcid.org/0000-0003-1619-3479
B. J. Wilkes https://orcid.org/0000-0003-1809-2364
C. P. O'Dea https://orcid.org/0000-0001-6421-054X
J. Kuraszkiewicz https://orcid.org/0000-0001-5513-029X
G. R. Tremblay https://orcid.org/0000-0002-5445-5401
A. Capetti https://orcid.org/0000-0003-3684-4275
B. Balmaverde https://orcid.org/0000-0002-0690-0638

References

Allen, M. G., Sparks, W. B., Koekemoer, A., et al. 2002, ApJS, 139, 411
Babyk, I., Melnyk, O., & Elyiv, A. 2012, AASP, 2, 188
Baldi, R. D., Chiaberge, M., Capetti, A., et al. 2010, ApJ, 725, 2426
Balmaverde, B., Capetti, A., Marconi, A., et al. 2019, A&A, 632, A124
Baum, S. A., Zirbel, E. L., & O'Dea, C. P. 1995, ApJ, 451, 88
Bennett, A. S. 1962, MmRAS, 68, 163
Bennett, C. L., Larson, D., Weiland, J. L., et al. 2014, ApJ, 794, 135
Best, P. N., & Heckman, T. M. 2012, MNRAS, 421, 1569
Bridle, A. H. 1984, AJ, 89, 979
Buttiglione, S., Capetti, A., Celotti, A., et al. 2009, A&A, 495, 1033
Chambers, K. C. & Pan-STARRS Team 2016, AAS Meeting Abstracts, 227, 324.07
Chiaberge, M., Capetti, A., & Celotti, A. 2000, A&A, 355, 873
Chiaberge, M., Capetti, A., & Celotti, A. 2002, A&A, 394, 791
Condon, J. J., Cotton, W. D., Greisen, E. W., et al. 1998, AJ, 115, 1693
D'Abrusco, R., Álvarez Crespo, N., Massaro, F., et al. 2019, ApJS, 242, 4

D'Abrusco, R., Massaro, F., Paggi, A., et al. 2014, ApJS, 215, 14
Dasadia, S., Sun, M., Morandi, A., et al. 2016, MNRAS, 458, 681
de Koff, S., Baum, S. A., Sparks, W. B., et al. 1996, ApJS, 107, 621
Edge, D. O., Shakeshaft, J. R., McAdam, W. B., et al. 1959, MmRAS, 68, 37
Fabian, A. C. 2012, ARA&A, 50, 455
Fanaroff, B. L., & Riley, J. M. 1974, MNRAS, 167, 31
Fitzpatrick, E. L., & Massa, D. 2007, ApJ, 663, 320
Freeman, P., Doe, S., & Siemiginowska, A. 2001, Proc. SPIE, 4477, 76
Fruscione, A., McDowell, J. C., Allen, G. E., et al. 2006, Proc. SPIE, 6270, 62701
Giovannini, G., Cotton, W. D., Feretti, L., et al. 2001, ApJ, 552, 508
Glowacki, M., Allison, J. R., Sadler, E. M., et al. 2017, MNRAS, submitted (arXiv:1709.08634)
Hardcastle, M. J., Evans, D. A., & Croston, J. H. 2009, MNRAS, 396, 1929
Hardcastle, M. J., Massaro, F., & Harris, D. E. 2010, MNRAS, 401, 2697
Hardcastle, M. J., Massaro, F., Harris, D. E., et al. 2012, MNRAS, 424, 1774
Hardcastle, M. J., Worrall, D. M., Birkinshaw, M., et al. 2005, MNRAS, 358, 843
Hickox, R. C., & Markevitch, M. 2006, ApJ, 645, 95
Hine, R. G., & Longair, M. S. 1979, MNRAS, 188, 111
Jimenez-Gallardo, A., Massaro, F., Paggi, A., et al. 2021, ApJS, 252, 31
Jimenez-Gallardo, A., Massaro, F., Prieto, M. A., et al. 2020, ApJS, 250, 7
Jones, L. R., Maughan, B. J., Ebeling, H., et al. 2004, in Clusters of Galaxies: Probes of Cosmological Structure and Galaxy Evolution, ed. J. S. Mulchaey et al. (Pasadena, CA: Carnegie Observatories), 25
Kalberla, P. M. W., Burton, W. B., Hartmann, D., et al. 2005, A&A, 440, 775
Kraft, R. P., Birkinshaw, M., Hardcastle, M. J., et al. 2007, ApJ, 659, 1008
Kraft, R. P., Birkinshaw, M., Nulsen, P. E. J., et al. 2012, ApJ, 749, 19
Laing, R. A., Jenkins, C. R., Wall, J. V., et al. 1994, in ASP Conf. Ser. 54, The First Stromlo Symp.: The Physics of Active Galaxies, ed. G. V. Bicknell et al. (San Francisco, CA: ASP), 201
Laing, R. A., Riley, J. M., & Longair, M. S. 1983, MNRAS, 204, 151
Liu, W., Sun, M., Nulsen, P. E. J., et al. 2020, MNRAS, 492, 3156
Liuzzo, E., Giovannini, G., Giroletti, M., et al. 2009, A&A, 505, 509
Madrid, J. P., Chiaberge, M., Floyd, D., et al. 2006, ApJS, 164, 307
Madrid, J. P., Donzelli, C. J., Rodríguez-Ardila, A., et al. 2018, ApJS, 238, 31
Magnier, E. A., Schlafly, E. F., Finkbeiner, D. P., et al. 2020, ApJS, 251, 6
Martel, A. R., Baum, S. A., Sparks, W. B., et al. 1999, ApJS, 122, 81
Maselli, A., Massaro, F., Cusumano, G., et al. 2016, MNRAS, 460, 3829
Massaro, F., Harris, D. E., & Cheung, C. C. 2011, ApJS, 197, 24
Massaro, F., Harris, D. E., Liuzzo, E., et al. 2015, ApJS, 220, 5
Massaro, F., Harris, D. E., Tremblay, G. R., et al. 2010, ApJ, 714, 589
Massaro, F., Harris, D. E., Tremblay, G. R., et al. 2013, ApJS, 206, 7
Massaro, F., Masetti, N., D'Abrusco, R., et al. 2014, AJ, 148, 66
Massaro, F., Missaglia, V., Stuardi, C., et al. 2018, ApJS, 234, 7
Massaro, F., Tremblay, G. R., Harris, D. E., et al. 2012, ApJS, 203, 31
McCarthy, P. J., Miley, G. K., de Koff, S., et al. 1997, ApJS, 112, 415
McMullin, J. P., Waters, B., Schiebel, D., et al. 2007, in ASP Conf. Ser. 376, Astronomical Data Analysis Software and Systems XVI, ed. R. A. Shaw et al. (San Francisco, CA: ASP), 127
Mingo, B., Croston, J. H., Hardcastle, M. J., et al. 2019, MNRAS, 488, 2701
Oke, J. B., & Gunn, J. E. 1983, ApJ, 266, 713
Orienti, M., Prieto, M. A., Brunetti, G., et al. 2012, MNRAS, 419, 2338
Paggi, A., Massaro, F., Pena-Herazo, H. A., et al. 2021, A&A, 647, A79
Pracy, M. B., Ching, J. H. Y., Sadler, E. M., et al. 2016, MNRAS, 460, 2
Privon, G. C., O'Dea, C. P., Baum, S. A., et al. 2008, ApJS, 175, 423
Ramírez, E. A., Aretxaga, I., Tadhunter, C. N., et al. 2017, FrASS, 4, 52
Ricci, F., Lovisari, L., Kraft, R. P., et al. 2018, ApJ, 867, 35
Schlafly, E. F., & Finkbeiner, D. P. 2011, ApJ, 737, 103
Spinrad, H., Djorgovski, S., Marr, J., et al. 1985, PASP, 97, 932
Stuardi, C., Missaglia, V., Massaro, F., et al. 2018, ApJS, 235, 32
Taylor, M. B. 2005, in ASP Conf. Ser. 347, Astronomical Data Analysis Software and Systems XIV, ed. P. Shopbell et al. (San Francisco, CA: ASP), 29
Tremblay, G. R., Chiaberge, M., Sparks, W. B., et al. 2009, ApJS, 183, 278
Wilkes, B. J., Kuraszkiewicz, J., Haas, M., et al. 2013, ApJ, 773, 15
Worrall, D. M., Birkinshaw, M., Hardcastle, M. J., et al. 2001, MNRAS, 326, 1127
Wright, E. L., Eisenhardt, P. R. M., Mainzer, A. K., et al. 2010, AJ, 140, 1868
Zhu, Z., Xu, H., Wang, J., et al. 2016, ApJ, 816, 54